Advancing Deep Hyperthermia: the design and realisation of a Microwave Tomography and Hyperthermia treatment system

Matthijs J.A. Jansen

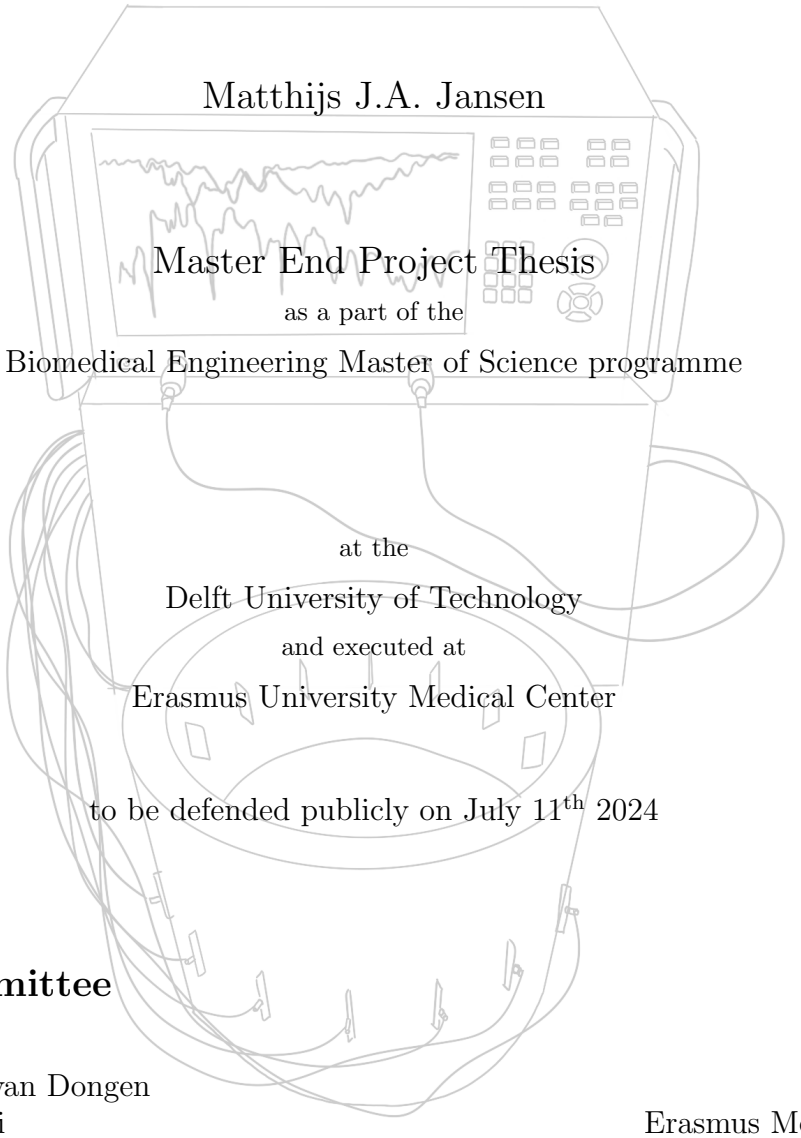

Master End Project Thesis

as a part of the

Biomedical Engineering Master of Science programme

at the

Delft University of Technology

and executed at

Erasmus University Medical Center

to be defended publicly on July 11th 2024

Thesis Committee

Dr. K.W.A. van Dongen	TU Delft
Dr. M. Zanoli	Erasmus Medical Center
Prof. Dr. B. Rieger	TU Delft
Dr. ir. N. Tümer	TU Delft

TU Delft Delft University of Technology

Erasmus MC Universitair Medisch Centrum Rotterdam

Abstract

This thesis is concerned with the technical, physical and computational challenges regarding the incorporation of microwave tomography in hyperthermia treatments. Hyperthermia is a clinical technique in which tumorous tissue is heated to gain therapeutic effect for concurrent radiotherapy. Hyperthermia by microwaves, as performed at the Erasmus Medical Center, suffers from uncertainties and lacking control. To relieve the burden of uncertainties regarding dielectric properties and patient positioning, microwave tomography can be used in hyperthermia systems. This could also improve treatments, as it would offer more possibilities for controlling the delivery. This work is focused on relieving several practical limitations to the integration of tomography, rather than researching its possibilities. This thesis is accompanied by the literature research "Advancements in Microwave Tomography and Hyperthermia Treatments" by the same author.

Acknowledgements

This work was conducted with the help of several members of the Erasmus MC's Department of Radiotherapy and specifically the Hyperthermia Unit. Special thanks go to my daily supervisor Dr. Max Zanoli for designing the multidisciplinary and challenging project. Furthermore, thanks go to Dr. Koen W.A. van Dongen, for encouraging discovering the subjects that lay in the author's personal interest. Moreover, the author would like to thank Prof. Dr. Bernd Rieger for being the chair and Dr. ir. Nazli Tümer for being a part of the thesis committee.

Other people who helped the author a lot are Dr. Sergio Curto, head of the Hyperthermia Unit, and Abi Kanagaratnam, MSc. Both participated in weekly update and outlook meetings, offering new insights into the project. From the TU Delft, the author would like to express thanks to Ronald Ligteringen and Roland Horsten. They helped to set up servers to do the extensive computations. Moreover, the author would like to express thanks to Sanne ten Hoopen for supporting him throughout the thesis and studies as a whole, lending a sympathetic ear and for the generation of the cover image. The author acknowledges the use of computational resources of the DelftBlue supercomputer, provided by Delft High Performance Computing Centre (https://www.tudelft.nl/dhpc).

Matthijs J.A. Jansen, June 2024

Contents

1. Introduction

1.1 Hyperthermia

Hyperthermia (HT) treatment is a therapy that dates as far back as ancient civilisations. Recent innovations have renewed the attention of the medical field to combat various health conditions. Hyperthermia is concerned with heating tissue, typically to a range of 40 °C to 45 °C, by which several heat-related effects happen in cells. Harnessing the heating creates a "focal point" of these effects. As so, diseased cells can be directly or indirectly eliminated and it is possible to spare healthy tissues in the neighbourhood.

Cancer treatment is one of the fields where hyperthermia is used to enhance the outcome of conventional therapies like radiation therapy (RT) and chemotherapy (ChT). Tumour cells are more sensitive to heat-induced stresses than healthy cells. On this basis, medical therapies focus on heating a specific body region or body part to higher temperatures and exploiting the tumour's vulnerability. Hereby, it becomes more sensitive to the harming mechanisms of RT or ChT. This effect is called sensitisation.

The approach of incorporating HT to get sensitising effects is called mild or synergistic hyperthermia. It is focused on improving the therapeutic impact and sparing healthy tissues. In the range above 45 °C, thermal ablation occurs. This means that cells are killed directly due to the heat. The synergistic effect is then minimal. Ablation is also known as moderate hyperthermia or thermal treatment and could be seen as burning the tissue. Lastly, HT can be used to release drugs locally. This is done with the use of thermosensitive liposomes (vesicles) with drugs inside. After administration of liposomes to the bloodstream, the drug release can be spatially targeted by HT, as the heat causes the liposomes to break down. Ablation and thermal targeting are out of the scope of this research.

The heat-related effects that hyperthermia induces are numerous and still further researched. They may enhance the outcome of RT, ChT or both up to some level[1]. The effects regard:

- Cytotoxic effects: Above 45°C and maintained for longer periods, exponential cell killing occurs. This is likely due to denaturation and aggregation of proteins.
- Effect on DNA repair: DNA repair proteins become inactive when exposed to heat [2]. Also, 'S'-phase cells are sensitised, whereas they are normally more guarded against DNA damage. Thermoradiobiologically, HT can therefore enhance low-LET radiation (X- and gamma rays). Low-LET radiation induces mostly single-strand breaks in the DNA, but under HT, these become the more lethal double-strand breaks because of the lack of repair mechanisms.

- Cellular membrane permeability: Due to the heat, the cell membrane will become more permeable.
- Immune system activity: Like a fever, hyperthermia stirs up the immune system. Increased activity together with other treatments (also immunotherapy) may be synergetic [2].
- Effects on tumour microenvironment:
  - Increased oxygenation: Hypoxic areas appear in solid tumours because of poor diffusion and limited oxygen supply. Hypoxic cells are more radioresistant, but this can be negated by increased oxidation to these areas under HT.
  - Vasculature and perfusion: The primitive construction of tumour vessels results in these vessels being more permeable than normal tissue vessels. With increased heat, these vessels will widen at first but later be obstructed due to poor organization [2].
- Thermotolerance effects/heat-induced stress: Heat Shock Proteins (HSP) are generated and activated by a cell under heat stress and they protect (tumour) cells from protein denaturation. Tumours with high levels of HSPs are less sensitive to heat. This makes them indirectly harder to kill, as it is not possible to sensitise them with HT. HSP inhibitors are developed to re-sensitize tumour cells for HT and subsequently, RT or ChT [2].

As already briefly mentioned, synergistic HT for RT mainly relies on the effects of DNA-repair inhibition, increased oxidation and heat-induced stress. For ChT, increased perfusion and membrane permeability are valued reactions. The effects are also still investigated, as they likely combine in a complex manner to make synergistic HT the potent sensitiser it is. The effects are mostly long-lasting, up to several days[3]. For that, HT only has to be applied once or twice a week, affecting other RT treatments during the week as well.

Innovations of several medical technologies, particularly regarding imaging modalities, improved the application of HT. Yet, precision in the delivery of hyperthermia treatments remains a pitfall. Targeted (the right area), controlled (not too much heat) and controllable (measure the heat) delivery all face challenges as well. Advanced heat-delivery applications could be realised with the incorporation of new imaging modalities. The increased accuracy will allow for controllable and reproducible heating procedures, which are hoped to improve therapeutic outcomes and limit damage to healthy tissue. Hyperthermia has still failed to become standard practice in the oncology community due to

- low temperatures achieved in patients, varying largely between patients and treatments,
- problems with steering and controlling HT treatments accurately,
- difficulties in generating HT equipment tailored to specific body parts,
- problems with accurate planning and dealing with uncertainties,
- absence of consensus on HT treatment planning and software,
- problems with accurate thermometry and quality assurance,

- a lack of randomised, large clinical trials for different tumour sites.

In the remainder of this paragraph, we will elucidate these issues.

For the application of HT, several implementations can be used. For this research, we are concerned with deep HT using external electromagnetic (EM) waves, as used at the EMC. This type of application can be planned upfront, which is one of the differences with respect to passive applications and superficial treatments. For treatments, the patients lay in an applicator with a number of antennas (called the array) in a water-filled sack (called the bolus) that makes contact with the patient. Both array and bolus design are important for the proper delivery of a treatment. There are different applicators for different parts of the human body. For different applicators, different EM wave frequencies are used. They are in the range of hundreds of MHz, with 434 MHz being the most common and also the one used in this research.

For EM (micro- and RF waves), wave interference is utilised to heat target regions positioned deeper into the body. Interference is the phenomenon that coinciding waves can be "summed", leading to a stronger wave. This interference can be simulated in treatment planning software to create accurate regional heating plans. Planned external hyperthermia utilizing EM waves is therefore the state-of-the-art method. In essence, the goal is to generate a set of amplitudes and phases for all the antennas in the array. This set should be such that radiating the antennas with those settings will yield the highest interference in the target region, leading to the largest temperature increase. However, as will be elaborated upon later in this paragraph, interference and temperature do not map one-to-one.

Hyperthermia planning normally follows the same order of actions, being:

1. patient imaging,
2. segmentation,
3. model generation,
4. EM, SAR (explanation below) and thermal calculations,
5. optimisation,
6. translation to the clinic.

See also Figure 1.1. In the first row, the patient segmentation can be found. On the second and third rows, the SAR and thermal calculation steps can be found.

Planned HT treatments deal with quite some uncertainties. One of them is the setup errors, which entail the patient being poorly aligned with the applicator system, though these can be dealt with by using margins [4]. Moreover, blood perfusion is a cause of errors. Perfusion is the main reason internal temperatures are maintained around 36 °C to 37 °C, thus it is actively working against the applied heating. Perfusion is estimated in the planning, yet it is hard to gauge and can vary largely over time, making it one of the bigger and unsolved problems. Lastly, tissue-specific EM properties are assigned to the delineated tissues. These concern the electric permittivity and conductivity. The EM properties influence wave propagation and attenuation respectively, meaning they are both rather important. Currently, these

values are assigned from CT scans by database values (like IT'IS [5], [6]), but they can vary largely inter- and intra-patient. This can cause big discrepancies between the planned treatments and the physically delivered ones.

The specific absorption rate describes the rate of energy absorption by a material per unit mass. It is specifically designed for radio- and microwaves. It is defined as

$$SAR = \frac{1}{V} \int_V \frac{\sigma(\vec{r}) \|\vec{E}(\vec{r})\|^2}{\rho(\vec{r})} dV(\vec{r}), \tag{1.1}$$

where V is volume, σ is conductivity, $\vec{E}$ is the electric field strength and ρ is the mass density, all evaluated at the infinitesimal volume point $V(\vec{r})$ within the volume V. The $\|...\|^2$ denotes the Euclidian length of the vector. The unit for SAR is W/kg.

As can be seen above in equation (1.1), conductivity is used to determine SAR, whereas the permittivity of tissue influences the electric field strength.

Some planning systems focus on optimising the SAR distribution first, before moving on to temperature prediction. Thermal models take into account thermal properties, perfusion and cooling. Optimisation on temperature is computationally more expensive and not much better. SAR-based optimisation is simpler, and thereby faster, and still sufficiently accurate for HT planning purposes, though it does not map one-to-one to the temperature distribution [7]. This is mostly due to the lack of considering perfusion and cooling.

To control and assess the quality of the HT treatment, thermometry is crucial. This practice is the measurement of temperature in or outside the patient's body and can be either invasive or superficial. Thermal probes are frequently used, but also magnetic resonance (MR) thermometry has recently gained more attention. MR thermometry is a variation on magnetic resonance imaging (MRI), whereby a patient is imaged over time to grasp the temperature changes. It has the added benefit of giving a full spacial distribution of temperature, instead of only certain spots on a thermal probe. Unfortunately, MR thermometry still has to be improved to get the accuracy needed for HT [8].

More and more trials that combine HT with RT are being conducted. However, they often lack large patient pools, which decreases their impact and convincing power. The trials conducted so far have been mostly positive, as illustrated by the systematic analysis by Datta et al. [9] on head-and-neck cancer treatments. The results of clinical trials show an overall favouring of RT+HT as opposed to RT alone. The outcome of HT is correlated to the quality of the treatment. If applied correctly, it is estimated that HT can bring about a higher equivalent dose than that is delivered by RT alone [10], [11]. To illustrate this, a normal radiation dose and an equivalent dose with HT are depicted in rows four and five of Figure 1.1. In essence, this is "free" extra dose, as we do not harm healthy tissue under HT.

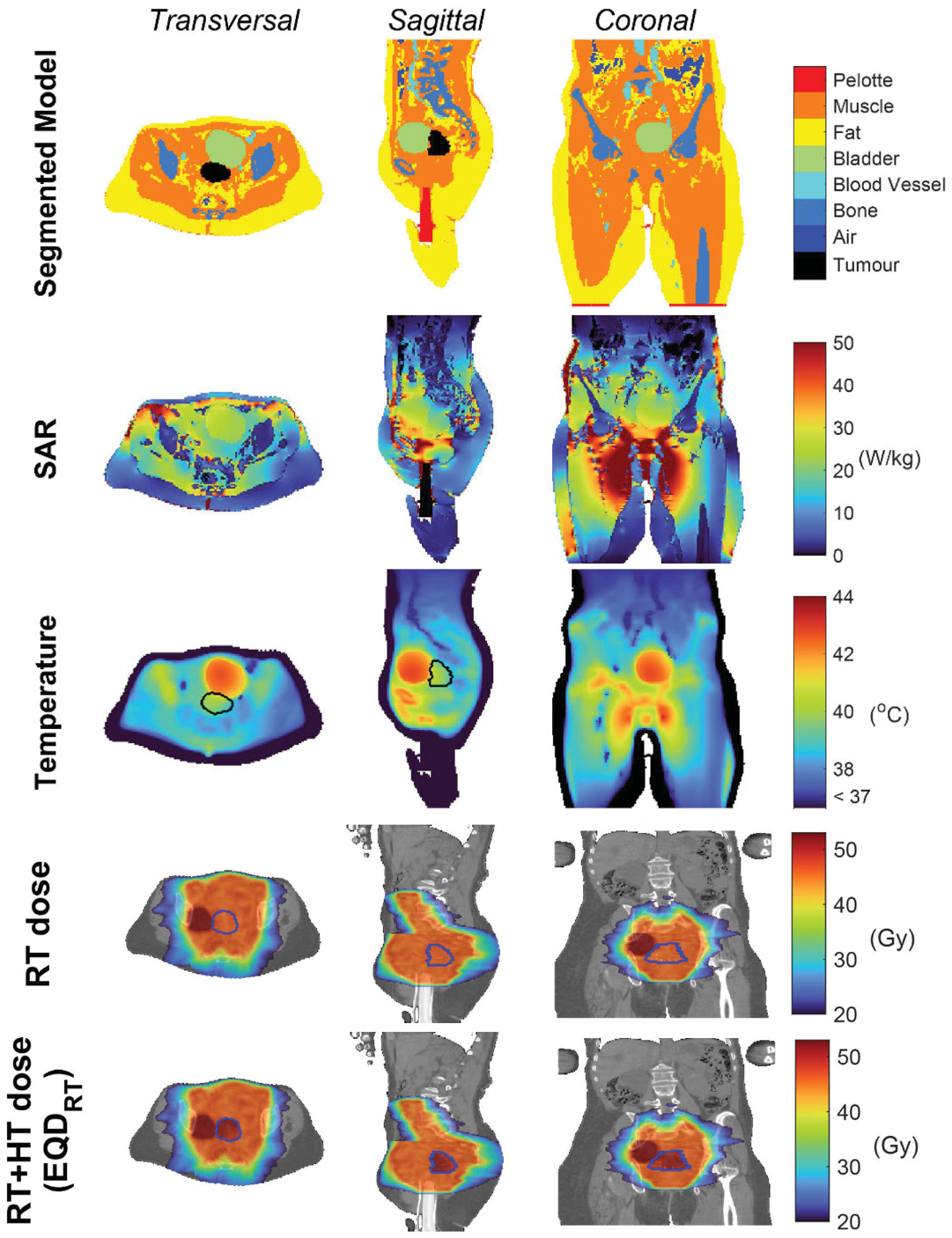

Figure 1.1: Different steps in hyperthermia treatment planning and effect evaluation. Each row depicts the transverse (axial), sagittal and coronal view of the abdomen of an HT patient. In the first row, a segmentation is made on the CT scan. The second row depicts the SAR values that came out of the treatment planning optimisation. Row three depicts the accompanying temperature distribution. In the fourth row, the plain RT dose is depicted. Lastly, in row five, the synergistic effect of HT+RT is depicted. Observe the added dose in the tumour, outlined in black and blue. Image taken and adapted from [12].

1.2 Microwave tomography

Microwave tomography (MT) is a medical imaging technique that can be used to assess internal body structures. Conventional techniques like X-rays, CT or MRI scans, cannot visualize the same properties as MT can, though they have a higher spatial resolution. Using EM waves at microwave frequency, non-invasive images of the dielectric properties of tissues can be realised by MT. These dielectric properties concern permittivity and conductivity, which were before mentioned to be the EM properties (EPs). Both EPs vary between tissue types and therefore MT allows for distinguishing organs at a rough scale and gives insight into their positions.

Microwaves are a type of EM radiation that has a non-ionizing frequency and energy level. This means that using microwaves for treatments or research won't expose patients or operators to harmful doses, making it safer than CT scans. Additionally, microwave tomography is fast and can be set up relatively inexpensively, which is a major advantage over MRI and CT scans. Microwaves can also penetrate deeper into tissues than ultrasound waves, giving rise to a larger field of view. However, microwave tomography has limitations such as low resolution (due to the diffraction limit) and challenges when imaging bony or air-filled tissues [13]. The process of reconstructing an image in microwave tomography poses an ill-posed inversion problem, leading to various issues that will be discussed later [14], [15].

The working principle of microwave tomography is the interaction between microwave signals and biological tissues. These waves penetrate the body depending on the dielectric properties per tissue. As they pass through the body, differing dielectric properties cause scattered and transmitted waves. All the scatterings and other alterations in the wavefield can be used to reconstruct the distribution of what must be the object transversed, the body. A graphical representation is depicted in Figure 1.2. It is important to note that all antennas in the array are both receiver and transmitter. This makes for a compact system, which is not very expensive to fabricate.

This research is concerned with microwave tomography, and not with microwave radar imaging. Microwave radar imaging is used for remote sensing, communication, or navigation and is a qualitative (detecting) method. Tomography is a quantitative method, meaning we can retrieve the values of the dielectric properties and get an EP distribution of the tissue. The electric permittivity, ϵ [Farad/meter, F/m] describes how a material polarises under exposure to an EM field. The electric conductivity, σ [Siemens/meter, S/m], describes how much of an EM wave energy is absorbed, and together they influence the speed and attenuation of an EM wave respectively. More on this will follow in Electromagnetic Scattering.

The research group led by Paul Meaney at Dartmouth College in the United States has produced the most developments regarding MT. After the introduction of the computational version of MT by Joachimovic [16], Meaney brought about improvements in the inversion algorithm, forward modelling techniques and measurement equipment [17], [18], [19]. The upgrade from 2D to 3D was later realised due to updated computational capabilities [20]. The first clinical experiments with MT were reported in the year 2000 when Meaney's group developed a system to analyse breasts [21]. This would evolve into a detection and screening

system for breast cancer since the breast is easily accessible and rather homogeneous. MT also received interest in lung, cardiac and brain imaging [14].

By 2010, it was discovered that the contrast between breast tissue and malignancies was not as high as anticipated. Thus, MT could not be utilised as a screening tool [22]. Clinical studies with microwave imaging have only been conducted four times from 2013 to 2017, often with small patient groups, and only two used MT [23]. Radar-based imaging techniques currently undergo large-scale clinical trials in Asia [24].

Hardware and software (computation) are two pillars that determine the quality of MT. For hardware, we regard the imaging tank, a coupling medium, the antenna array and signal processing systems. On the software side, we consider the inversion and the forward modelling. Together, they yield the reconstruction.

The imaging tank in its simplest form is a water bath. It needs to provide space for both the object and the antenna array in the most optimal (for measurements) configuration. Moreover, it needs to be relatively comfortable for the patient. The coupling medium (CM) is the liquid that is placed in the measuring device to better propagate the EM waves to the object and back to the antennas. Water is often used, possibly with salt or glycerol to increase the conductivity. Multipath waves are the signals that scatter multiple times before being registered, which makes it harder to invert or even impossible with certain inversion schemes. Increasing the conductivity of the CM attenuates these waves sufficiently for the reconstruction to converge again [25]. Lastly, the signal processing systems need to be sensitive to small disruptions in signal, as the scattered signal is orders of magnitude smaller than the transmitted signal. Therefore, antennas, cables and measurement equipment have to be of high quality and preferably be characterized/calibrated. Eventually, the measurements from these antennas feed the reconstruction, so accuracy is key.

To get an image of the EP distribution, inversion and forward modelling are used in alternating fashion. In essence, the algorithm is constantly guessing the answer, calculating the error to the measured data and making a better guess again based on the error. Forward modelling takes the input source and produces an artificial output dataset from its model. This can be done with finite element (FE) or finite difference time domain (FDTD) models. The inversion takes an output dataset and tries to reconstruct an input model that fits the measured datasets. Algorithms for this include (Bi-)Conjugate Gradient, Born Inversion, Full Wave Inversion and Constrast-Source Inversion. Updating the guess based on the error is done per an iteration scheme. Most methods employ a (modified) Gauss-Newton iterative scheme. As the electric field is sampled at a limited amount of points (the antennas) outside the object, reconstruction inside the object is ill-posed. That means that we will theoretically have more than one solution, no solution, the solution is unstable or the solution is not unique for all data points.

1.3 Outline

This thesis is concerned with the development of a microwave tomography system within a hyperthermia treatment system. As the method for the reconstruction of a tomography image has already been developed, this work is focused more on the practical implementation of such a method.

Despite advancements in HT, clinical trials and treatment outcomes are lacking or underperforming. Patient positioning and EP uncertainties likely underlay this problem. Microwave tomography can remove these hurdles and allow for more control of the treatments. Thus far, MT has only been attempted to be used as a diagnostic tool, which proved unsuccessful. Yet, we aim to use it as a support tool, which could give real-time insight, despite its shortcomings. MT and HT can make use of the same, relatively cheap, setup, but not without some adjustment. A prominent problem is the difference in the CM in MT versus HT, as the former has previously been done with lossy media, and the latter requires almost loss-less media. Also, MT uses sensitive, low-power equipment, whereas HT uses high-power amplifiers. These issues pose challenges on both the hardware and software sides.

The core goal of this research is concerned with the question: **"Developing a dual-functionality system that allows for both hyperthermia treatment and microwave tomography"**

As stated before, this project aims to tackle different problems posed by the physical integration of MT and HT. Therefore, it might feel to the reader as if several separate projects are tied together. In practice, however, it will be a series of hurdles, each of which presents itself after another is solved. To the end of integrating MT, a switching matrix and software part will be developed to acquire data swiftly and guard the sensitive equipment of MT. Moreover, the possibilities for hardware and signal processing will be explored, to maximise data quality. A new imaging setup will be generated, to make optimal use of the CM and array. By the development of these systems and identifying their pitfalls, it is hoped to improve the accuracy and quality of synergetic hyperthermia treatments. Eventually, the addition of microwave imaging as a medical imaging tool could thereby improve clinical outcomes. Though not explored in this project, MT could also prove to be beneficial for other types of hyperthermia, or even other applications unbeknownst for now.

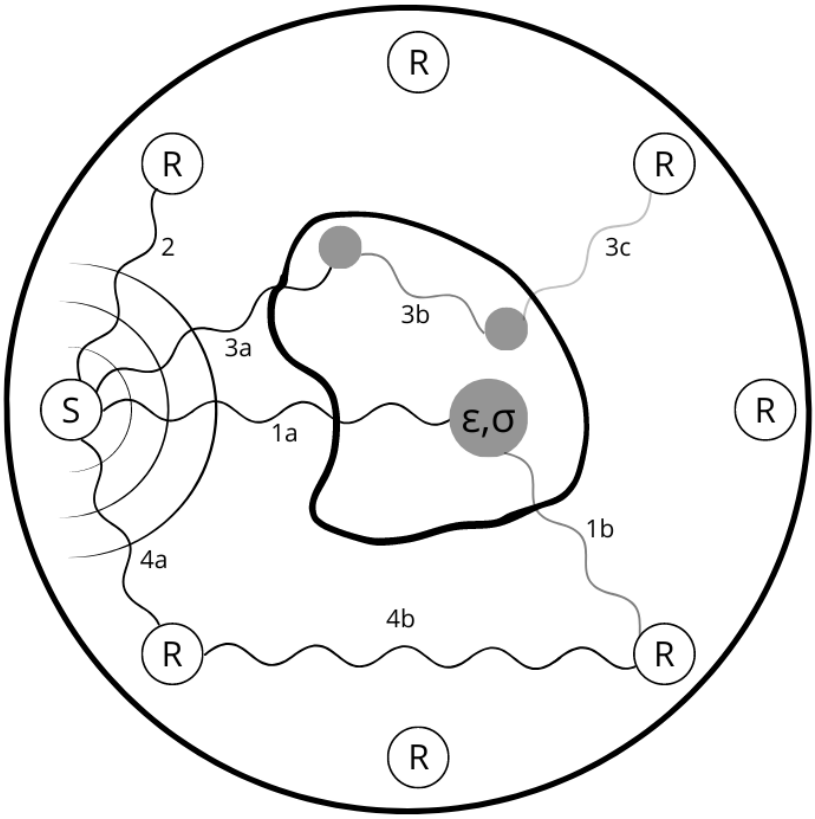

Figure 1.2: Principle of microwave tomography. Within the circular imaging tank, eight antennas are placed. One of these (S) will send out EM waves, which the others (R) will receive. The object in the middle will cause scattering, wave attenuation and phase shift according to its EPs (ϵ, σ). Wave 1a will be scattered to wave 1b, which has a decreased amplitude depicted by the lower intensity. Other waves, such as wave 2, are not travelling through the object, meaning the wave will be wholly transmitted to the receiver antenna. Wave 3a is scattered multiple times to waves 3b and 3c respectively. This will cause a very low-intensity wave to be received, possibly too weak to be detected at all. Note that multiple scatters can also include interactions at the boundary of the tank. Lastly, wave 4a incidents on a receiver antenna, which will cause it to be excited due to reciprocity. A strong wave 4b will be transmitted to another receiver antenna, possibly disrupting its detection of object-scattered waves.

2. Theory

2.1 Scattering and Acquiring Signal

This chapter will elucidate some theoretical and physical aspects of relevant subjects. The scattering and propagation of EM waves will be discussed, as well as some notes on signal acquisition. The second part will discuss what the mathematical foundation is for translating a measurement into an image.

Electromagnetic Scattering
EM waves travel through any medium depending on the medium's permittivity and permeability. The permittivity ϵ [F/m] can be described as the extent to which a medium can be polarized. The permeability μ [H/m] is the extent to which a medium can be magnetized. Together, they describe how easy it is for an electric or magnetic field to travel through a medium. The relationship to the speed of light c is defined as

$$c = \frac{1}{\sqrt{\epsilon\mu}}. \tag{2.1}$$

For most biological tissues and for water, $\mu \approx \mu_0$. This means that the permeability is roughly the permeability of vacuum, μ_0. In the context of this research, we will therefore regard (2.1) as

$$c(\epsilon, \mu) = c(\epsilon) = \frac{1}{\sqrt{\epsilon\mu_0}}. \tag{2.2}$$

The relative permittivity, ϵ_r [-] is the ratio of the permittivity in the material to the permittivity in a vacuum, ϵ_0, and is sometimes also used to simplify comparisons. Both ϵ and μ depend on the temperature of the medium and the EM wave's frequency. As this research concerns only one frequency and mostly at room temperature, we disregard this influence. Please note that when moving on to hyperthermia treatments, the temperature will increase. The temperature dependence of ϵ is considerable [26]. However, in hyperthermia with small temperature increments (in the order of a couple of degrees), the impact of these variations is minimal.

The electric conductivity σ [S/m] describes the ease with which an EM wave can travel through a medium. Thereby, it describes the energy transfer of a wave to a medium. The higher the conductivity, the easier it is for an electric field to generate an electric current, which in turn yields energy transfer. As it takes time for the polarization to be induced, conductivity brings about a complex factor in the previously defined permittivity. That is, the permittivity is dependent on the presented current. This relationship is related to the inverse of the angular

frequency ω. Complex permittivity can be defined as follows

$$\epsilon = \epsilon' + i\frac{\sigma}{\omega}, \tag{2.3}$$

where ϵ' is the real part of the permittivity, $i^2 = -1$ and where ω [rad/s] depicts the angular frequency $= 2\pi f$, with f [1/s, Hz] the frequency of the EM wave.

The wave impedance Z depicts the ratio of the magnetic and electric phasors of an EM wave. These elements travel transverse to the wave's propagation direction. For transverse electromagnetic (TEM) waves, the electric and magnetic waves are orthogonal to one another. The electric impedance Z is given by

$$Z = \sqrt{\frac{i\omega\mu}{\sigma + i\omega\epsilon}} \tag{2.4}$$

It can be seen from equation (2.4) that the impedance is a complex number. Observe that for an ideal, loss-less dielectric (σ=0 S/m), the impedance is simply the square root of the permeability over the permittivity.

At interfaces of materials with a different impedance, reflection will occur. At irregular interfaces or in a heterogeneous medium, this will be perceived as scattering. The larger the difference in impedance, the larger the scattering effect. To this end, impedance matching can be used for heterogeneous media to limit reflective losses. For example, a coupling medium can be used to bridge the impedance gap of various materials.

When looking at a larger domain, we can describe the total electric field as the vector field $\vec{E}_{tot}$. The total field is the same field that one could measure if desired. When undisturbed, the (artificially) generated field $\vec{E}_{inc}$ corresponds to $\vec{E}_{tot}$. However, when an object with a different impedance is presented, a scattered field will arise from the incident field. This can be described as

$$\vec{E}_{tot} = \vec{E}_{inc} + \vec{E}_{sca}, \tag{2.5}$$

where $\vec{E}_{sca}$ depict the scattered electric field. Note that an EM wave could scatter multiple times within an object. Therefore, the scattered field can be best described as an integral of the individual scattering events summed. To come to this formulation, we first need to define the dyadic Green's function $G(\vec{r}, \vec{r}\,')$. The Green's function is the response of the entire domain to a single impulse signal coming in. We can regard any signal as a sum of impulses, and therefore we can use Green's function to describe the whole response. The dyadic Green's function is defined here as

$$\nabla \times \nabla \times G(\vec{r} - \vec{r}\,') - \frac{\omega^2}{c^2} G(\vec{r} - \vec{r}\,') = I\delta(\vec{r} - \vec{r}\,'), \tag{2.6}$$

where $\nabla\times$ is the curl operator, I is the identity matrix and $\delta(\vec{r}-\vec{r}\,')$ is the Dirac delta function. The location vectors $\vec{r}$ and $\vec{r}\,'$ depict the current location and response location, respectively. Hereby, the Green's function describes the extent to which a scattering event at $\vec{r}\,'$ has an influence on the field at $\vec{r}$. We can now define the scattered field as a function of time and

place, hence

$$\vec{E}_{sca}(\vec{r},t) = \omega^2 \int_{V(\vec{r}\,')\in D} G(\vec{r}-\vec{r}\,')\,\chi(\vec{r}\,')\,\vec{E}_{tot}(\vec{r},t)\,dV(\vec{r}\,'), \tag{2.7}$$

where we introduced the contrast term $\chi(\vec{r}\,')$ to account for the spatial variation in the speed of light $c(\vec{r}\,')$. The contrast term is defined as

$$\chi(\vec{r}) = \frac{1}{c(\vec{r})^2} - \frac{1}{c_b^2}. \tag{2.8}$$

With this, we finally find that the total EM wave field equals

$$\vec{E}_{tot}(\vec{r},t) = \vec{E}_{inc}(\vec{r},t) + \omega^2 \int_{V(\vec{r}\,')\in D} G\,(\vec{r}-\vec{r}\,')\chi(\vec{r}\,')\vec{E}_{tot}(\vec{r},t)\,dV(\vec{r}\,'). \tag{2.9}$$

From (2.9), the total field on the left can be measured at the antennas. Moreover, the incident field is known from calculations or simulations. The Green's function can be calculated, which leaves the contrast term χ as the only unknown, together with $\vec{E}_{tot}(\vec{r},t)$ in the integral. The contrast term is of peculiar interest, as it describes the speed of light alterations, which are in turn governed by the alterations in EPs. However, to retrieve the contrast, we need the full distribution of the total electric field to evaluate the integral. This means that we need to alternate "guessing' the contrast and electric field to retrieve the other, which is done by iterative reconstruction. Different inversion techniques tackle this problem in different ways.

VNA and S-matrix

A Vector Network Analyser (VNA) is a measurement instrument that can be used to measure the transmission and propagation of an electric signal through an electric system, often called the Device Under Testing (DUT). For a simple DUT, a two-port VNA is sufficient, but four-port VNAs are also available. A VNA can analyse EM signals over a broad band of frequencies, where it measures phase and amplitude with high accuracy. Moreover, it can scan through a whole range of frequencies at a high rate, generating a frequency sweep measurement. Typical operating frequencies are in the order of kHz to GHz. Modern-day VNAs have a dynamic range (signal-to-noise ratio) of up to -120 dB.

VNAs are mainly used in research and calibration/verification of designed electrical systems such as amplifiers, antennas and cables. It is unique in the sense that is both the generator and receiver of the signal, as opposed to spectrum analyzers. So, it can do a complete measurement, with which a developer can determine if the response of a component matches its simulation and design characteristics. While the measurement makes use of the Fourier Transform, an Inverse Fourier Transform makes it possible to get time-domain responses [27].

Contrary to other measurement instruments, VNAs normally depict their readings as a ratio. That means that every measurement is relative to a certain set value. As the VNA is both the generator and receiver of the signal, the returning wave is normalized by the transmitted signal. We depict transmitted signals by a_i and reflected signals by b_i. Here, i is the index of the VNA port. It is common to quantify these waves a and b as the measured incoming or

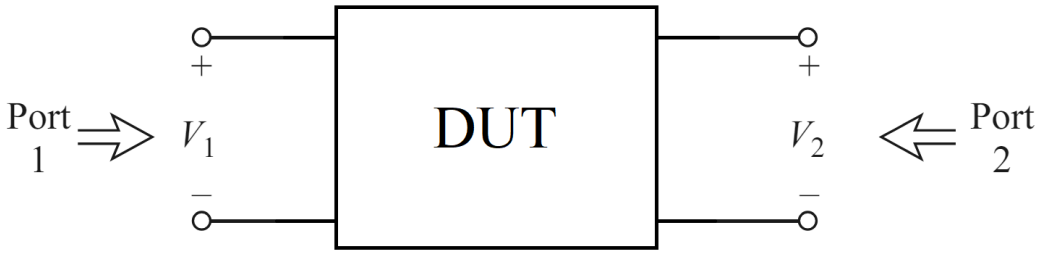

Figure 2.1: Schematical representation of a simple two-port network. The DUT in this setup will reflect and transmit both V_1^+ and V_2^+ up to some extent, which is quantified by measuring V_1^- and V_2^-. Image is taken and adapted from [28].

outgoing voltage at a port. Therefore, for a two-port network as in Figure 2.1, we define

$$\begin{aligned} a_1 &= V_1^+, & b_1 &= V_1^-, \\ a_2 &= V_2^+, & b_2 &= V_2^-. \end{aligned} \tag{2.10}$$

As can be seen, the ratio a_i/b_j for a fully reflected ($i = j$) or transmitted ($i \neq j$) wave will be 1. Be aware that this only holds for the magnitude of the wave, as it does not depict phase delay.

A simple depiction of multiple measurements is the Scattering matrix or S-matrix for short. This is an NxN matrix that holds the ratioed measurement for each combination of transmitting and receiving ports in an N-port network. For a two-port network, this grants the 2x2 S-matrix with the following values

$$\begin{bmatrix} S_{11} & S_{12} \\ S_{21} & S_{22} \end{bmatrix} = \begin{bmatrix} \frac{b_1}{a_1} & \frac{b_1}{a_2} \\ \frac{b_2}{a_1} & \frac{b_2}{a_2} \end{bmatrix}. \tag{2.11}$$

Note that the indices of the parameters S_{ij} in the S-matrix, the S-parameters, depict the receiving (i) and transmitting (j) port numbers. These again correspond with b_i and a_j, respectively. One crucial condition for determining these parameters is that only port j is transmitting. All other ports should be matched, so neither sending nor reflecting any signal. In that way, we measure the 'pure' reflection and transmission of ports i and j. In a mathematical formulation, this can be depicted as

$$S_{ij} = \frac{b_i}{a_j} = \frac{V_i^-}{V_j^+}\bigg|_{V_k^+=0 \text{ for } k\neq j}. \tag{2.12}$$

2.2 Signal Reconstruction and Inversion

De-embedding

In some cases, the DUT might not be suitable to directly connect to a VNA. There might be

a need for some additional cables, power amplifiers, attenuators, filters or other components to operate the DUT as intended. These components all have some influence on the attenuation and phase delay of a signal. If the influence is deemed insignificant, no further action is required. However, if these components result in a significant alteration of your signal, testing the DUT becomes cumbersome. To that extent, de-embedding can be used. The principle of de-embedding is that by characterizing all additional components themselves, their influence on the measurement with the DUT can be accounted for. Unfortunately, it is not as simple as taking the inverse or subtracting some S-matrix. That is because the S-matrices of different components "cascade", rather than multiply. This can be depicted as

$$\left[S_{total}\right] = \left[S_1\right] \otimes \left[S_2\right] \neq \left[S_1\right] \ \left[S_2\right] \tag{2.13}$$

The mathematical basis for de-embedding therefore comes from the ABCD matrix or transmission matrix. With ABCD matrices, it is possible to define the influence of a series of components as a series of matrices. See also Figure 2.2 Later, this can be used to remove the influence of either of them. The ABCD matrix relates voltages $V_{1,2}$ and currents $I_{1,2}$ at the two ports as

$$\begin{bmatrix} V_1 \\ I_1 \end{bmatrix} = \begin{bmatrix} A & B \\ C & D \end{bmatrix} \begin{bmatrix} V_2 \\ I_2 \end{bmatrix}. \tag{2.14}$$

If we now consider two components, we can consider a cascade of ABCD matrices. See Figure 2.3. As V_2 and I_2 are the output quantities of the first component and the input of the second component, it can be found with equation (2.14) that

$$\begin{bmatrix} V_1 \\ I_1 \end{bmatrix} = \begin{bmatrix} A_1 & B_1 \\ C_1 & D_1 \end{bmatrix} \begin{bmatrix} A_2 & B_2 \\ C_2 & D_2 \end{bmatrix} \begin{bmatrix} V_3 \\ I_3 \end{bmatrix}. \tag{2.15}$$

With equation (2.15), we can retrieve the characteristics of one of the components, if the other component and our measurements at the two ports are known. This can be done with left- or right-multiplication with the inverse of either ABCD matrix.

As we are interested in the S-matrix and not the ABCD matrix, we need to interchange between the two [28]. Without extensive derivation, we will proceed to formulate the relationship between S- and ABCD parameters

$$\begin{aligned} A &= \frac{(1+S_{11})(1-S_{22})+S_{12}S_{21}}{2S_{21}}, & S_{11} &= \frac{A+B/Z_0-CZ_0-D}{A+B/Z_0+CZ_0+D}, \\ B &= Z_0\frac{(1+S_{11})(1+S_{22})-S_{12}S_{21}}{2S_{21}}, & S_{12} &= \frac{2(AD-BC)}{A+B/Z_0+CZ_0+D}, \\ C &= \frac{1}{Z_0}\frac{(1-S_{11})(1-S_{22})-S_{12}S_{21}}{2S_{21}}, & S_{21} &= \frac{2}{A+B/Z_0+CZ_0+D}, \\ D &= \frac{(1-S_{11})(1+S_{22})+S_{12}S_{21}}{2S_{21}}, & S_{22} &= \frac{-A+B/Z_0-CZ_0+D}{A+B/Z_0+CZ_0+D}. \end{aligned} \tag{2.16}$$

Here, Z_0 is the characteristic impedance of the system. This is typically 50 Ohm.

Ill-posed Inversion

Recovering any set of unknowns is possible when just as many independent equations are known. However, if the set of unknowns is (much) bigger than the known values or equations,

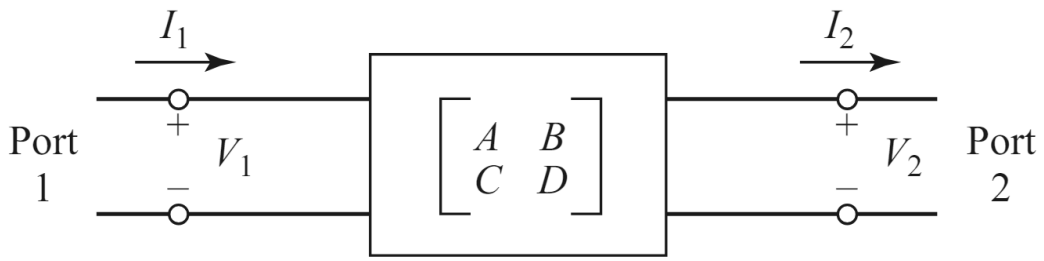

Figure 2.2: Depiction of a two-port network with the DUT depicted as the ABCD-matrix. Image is taken from [28].

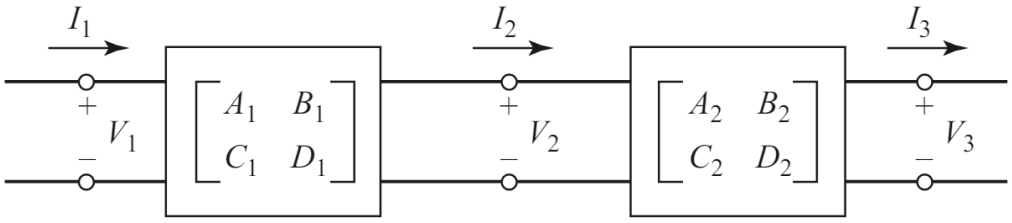

Figure 2.3: Depiction of a two-port network with components and intermediate voltage V_2 and current I_2. Both components are depicted as their ABCD-matrix. Image is taken from [28].

the problem is underdefined. In the context of this research, the amount of measured values (the amount of antennas) is only a whim of the amount of voxels that are sought to be reconstructed. Therefore, we speak of an ill-posed inversion problem. Tackling these problems can be done with various inversion algorithms. Among them are Born Inversion, Contrast Source Inversion and Full Wave Inversion. In this research, an in-house method is employed, relying on the Biconjugate gradient and adjacency matrix. To this end, equation (2.9) is written as a matrix multiplication. Therefore, we discretize the spatial domain into G cubic elements, which are illuminated using P antennas, resulting in $P \times P$ measurements. We can define matrix $\mathbf{E}$ as

$$\mathbf{E} = \begin{bmatrix} \mathbf{E}_1 \, \mathbf{E}_2 \, \cdots \, \mathbf{E}_P \end{bmatrix}, \quad \mathbf{E}_a = \begin{bmatrix} \mathbf{e}_{1a} \\ \mathbf{e}_{2a} \\ \vdots \\ \mathbf{e}_{Ga} \end{bmatrix}, \quad \mathbf{e}_{ga} = \mathbf{e}_a(\vec{r}_g), \tag{2.17}$$

where $\mathbf{E}_a$ depicts the electric field when port a is radiating. $\mathbf{e}_a(\vec{r}_g)$ depicts the electric field at point $\vec{r}_g$, where g indicates the grid element index. Likewise, we define the matrix $\bar{\mathbf{E}}$ to describe the fields measured at the antennas as

$$\bar{\mathbf{E}} = \begin{bmatrix} \bar{\mathbf{E}}_1 & \bar{\mathbf{E}}_2 & \cdots & \bar{\mathbf{E}}_P \end{bmatrix}, \quad \bar{\mathbf{E}}_a = \begin{bmatrix} \bar{\mathbf{e}}_{1a} \\ \bar{\mathbf{e}}_{2a} \\ \vdots \\ \bar{\mathbf{e}}_{Pa} \end{bmatrix}, \quad \bar{\mathbf{e}}_{pa} = \mathbf{e}_a(\vec{r}_p). \tag{2.18}$$

These entries are indexed with p, and $\vec{r}_p$ describes the antenna's probe point. In discrete form, the contrast term will read

$$\mathbf{Q} = \begin{bmatrix} \boldsymbol{\chi}_1 & \cdots & \mathbf{0} \\ \vdots & \ddots & \vdots \\ \mathbf{0} & \cdots & \boldsymbol{\chi}_G \end{bmatrix}, \tag{2.19}$$

where $\boldsymbol{\chi}_g$ is a 3x3 diagonal matrix with entries $\chi(\vec{r}_g)$ and $\mathbf{0}$ is a 3x3 matrix with all entries 0. Finally, the integral over the whole domain needs to be discretized. We define matrix $\mathbf{M}$ as

$$\mathbf{M} = \begin{bmatrix} \mathbf{m}_{11} & \cdots & \mathbf{m}_{1G} \\ \vdots & \ddots & \vdots \\ \mathbf{m}_{G1} & \cdots & \mathbf{m}_{GG} \end{bmatrix}, \mathbf{m}_{dg} = \frac{\omega^2}{c^2} \int_{\vec{\hat{r}}_g \in D} F(\vec{r}_d, \vec{\hat{r}}_g) d\vec{\hat{r}}_g, \tag{2.20}$$

where $\vec{\hat{r}}_g$ is the vector describing a discrete element g, as opposed to the infinitesimal point $\vec{r}$. Observe that $\mathbf{m}_{dg}$ is a 3x3 matrix, depicting the response in x, y and z to the origin point's field in x, y and z.

All together, we can now describe equation (2.5) as

$$\mathbf{E_{sca}} = \mathbf{MQE_{tot}}. \tag{2.21}$$

Similar to how (2.17) was transformed into (2.18) for the antenna points, we can transform (2.20) to the antenna point forms. We then get

$$\bar{\mathbf{E}}_{\mathbf{sca}} = \bar{\mathbf{M}}\mathbf{QE_{tot}}. \tag{2.22}$$

To conclude, we can use the normalized electric field matrices $\mathbf{E_{nor}}$ and $\bar{\mathbf{E}}_{\mathbf{nor}}$, which are described as

$$\mathbf{E_{nor}} = \frac{\mathbf{E_{sca}}}{\mathbf{E_{inc}}}, \tag{2.23}$$

$$\bar{\mathbf{E}}_{\mathbf{nor}} = \frac{\bar{\mathbf{E}}_{\mathbf{sca}}}{\bar{\mathbf{E}}_{\mathbf{inc}}}. \tag{2.24}$$

Then, we can define the cost function C as

$$C = \|\bar{\mathbf{E}}_{\mathbf{nor}} - \mathbf{E_{nor}}\|. \tag{2.25}$$

From our measurement, we retrieve the S-matrix. We can relate this to the voltage, and thereby the electric field at the antennas. Thus, we can acquire $\bar{\mathbf{E}}_{\mathbf{nor}}$. Via a reconstruction algorithm, $\mathbf{E_{nor}}$ can be iteratively guessed to minimise the cost function.

3. Materials

This chapter describes how different aspects of physical and computational research were set up. The chapter is split into a Hardware and a Software part.

3.1 Hardware

Vector Network Analyser

A VNA was used to acquire the scattering matrix, which depicts the received signal for each antenna when another one is radiating. The VNA employed was a Rohde-Schwarz ZNC3 [29]. This VNA can send out waves of 9 kHz to 3 GHz and has a characteristic impedance of 50 Ohm, similar to most other systems used in research. The acquired measurements were taken in the frequency range of 400 to 500 MHz with 101 samples. The measurements were not averaged. The duration of such a complete measurement, also called a single sweep, is roughly 0.6 seconds. The pure measurement for 120 channels would therefore be just over a minute.

Switching Matrix

A multiplexer or switching matrix (SwMat) was used to connect 16 antennas to the 2 available VNA ports. With this, a full 16x16 S-matrix could be filled. The SwMat can be seen in 3.1a. An Arduino Mega2560 steers the matrix. Furthermore, it consists of a series of step-up boards, to provide the 12 V that the switches need instead of the 5V provided by the Arduino. Each of the 16 entries consists of a High-Power Switch(HPS), which is needed to provide dual functionality, see Figure 3.1b and 3.1c. We want to use our applicator for heating and imaging, the former of which requires orders of magnitude more power than the latter. The HPSs shield the parts in the matrix that cannot handle these high powers. Four revolver switches with 8 outputs each (Single port 8 throw, SP8T) allow for each of the 16 incoming cables to be connected to either of the two ports that connect to the VNA, see Figure 3.1e and 3.1f. A series of 16 normal switches in between the HPSs and SP8Ts allow for sending each antenna to either of the 2 output ports, see Figure 3.1d. Two final SPDTs determine which of a pair of rotary switches' output goes through. Therefore, the switching matrix allows for a 2x8x2 multiplexing grid. The SP8T switches are matched, which means that the seven or all eight inputs that are not passing are terminated in a 50-Ohm impedance. To cool the SwMat during longer operation, a fan is incorporated. See also Appendix A for a schematic of the SwMat. One of the SP8T switches and its power cables were replaced because a faulty connection seemed to be made to port 11.

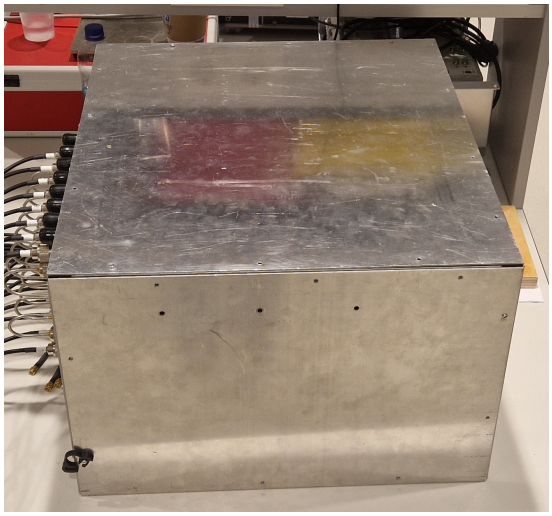

(a)

(b)

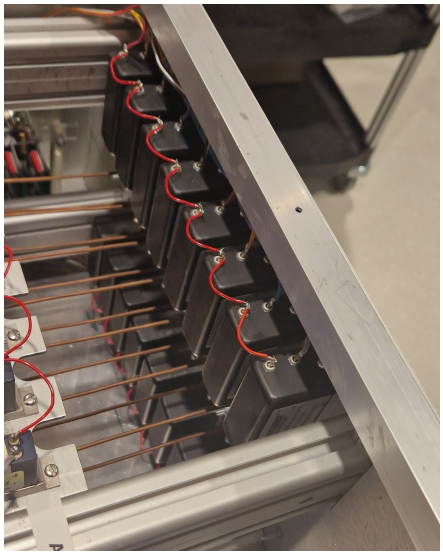

(c)

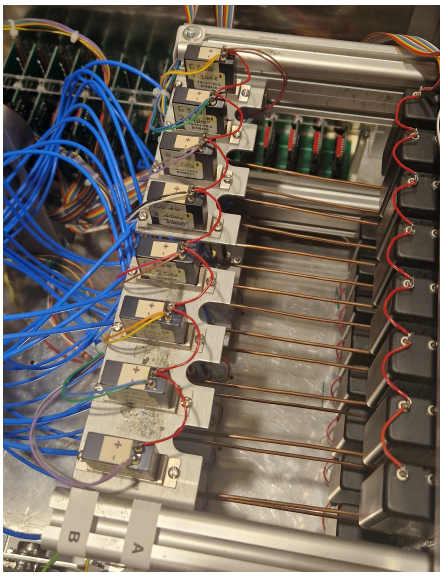

(d)

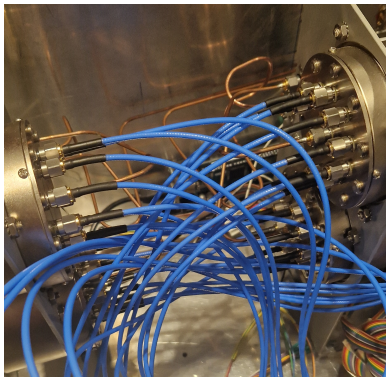

(e)

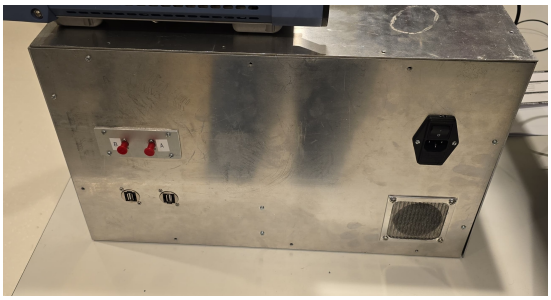

(f)

Figure 3.1: Images of Switching Matrix. (a): Full view. (b): Side with 16 antenna inputs. (c): 16 High Power Switches. (d): Top eight of 16 SPDTs. (e): Top two of four SP8Ts. (f): Side with two outputs as well as power, USB and fan inlet.

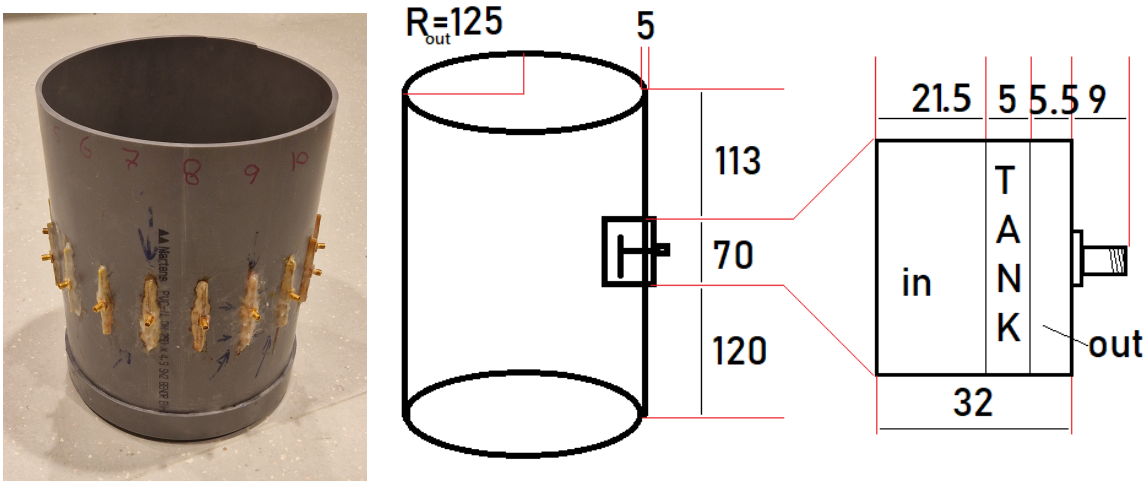

(a) (b)

Figure 3.2: Imaging Tank 1. (a): Side view. (b): Dimensions in mm

Connection cables

The connection from VNA to the switching matrix was made with two coaxial cables (coax). The connections of the switching matrix to the imaging tank were made with another 16 coaxes. All 18 coaxial cables were of the same type, being Kingsignal RG58 50 Ohm SMA (M) to N (M) 1.5 metres. At 434 MHz and 20 ^{o}C, it has a characteristic loss of 33.8 dB/100 m.

The steering of the hardware and the data acquisition from the VNA was done with a local computer. Connection to the VNA was made with a LAN cable. Connection to the Arduino with a USB cable to the USB port on the outside of the SwMat (see also Figure 3.1f).

Imaging Tank 1

The imaging tank used for the first experiments was previously built by another student. It concerns a 25 cm diameter PVC cylindrical pipe with 5 mm sides. On the bottom, a fitting 5 mm thick PVC cap was glued. The internal height is 30.7 cm. At 12 cm from the bottom, the antennas are placed. The antennas are 7 cm high, resulting in an antenna-to-top distance of 11.7 cm. A total of eighteen antennas are incorporated, evenly spaced every 20 degrees or approximately 4.37 cm apart on the circumference. The antennas are glued in place, also making the tank watertight. Moreover, the antennas were numbered for the sake of reproducibility and troubleshooting. An image of the tank can be found in Figure 3.2a. Schematics with dimensions can be found in Figure 3.2b. Antennas # 13 and # 16 were a bit leaky. Antennas # 7 and # 15 showed variant behaviour regarding reflection and stability. Different combinations of these antennas were omitted in all experiments, as only sixteen out of eighteen could be connected anyway.

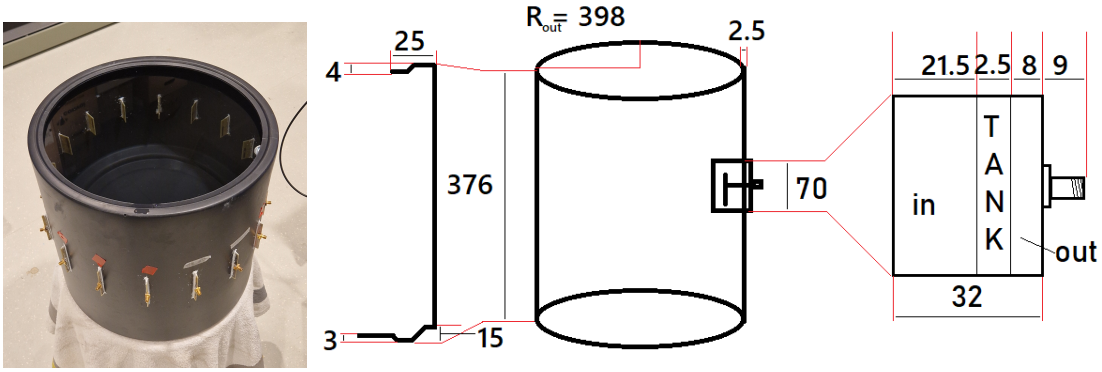

(a) (b)

Figure 3.3: Imaging Tank 2. (a): Side view. (b): Dimensions in mm.

Imaging Tank 2

Later in the project development, it was decided to break down the first imaging tank and build a new, larger one. Antennas were salvaged and cleaned from the old tank. The new tank was made out of a plastic (High-Density Polyethylene, HDPE) flower pot. Images can be found in Figure 3.3a and dimensions in Figure 3.3b. With a 39.8 cm diameter, it is significantly larger than the first tank. Also, with a 3 mm thickness, it is thinner. More differences include the integrated bottom, as opposed to the glued-on cap, and a small brim on top. It is expected that neither of these alterations makes the new tank less suited, even more so because of the bigger size and longer path lengths. By that, the antennas behave more in the "far-field", which is easier to accurately model and the antennas are further away from each other, which decreases unwanted coupling. In line with the SwMat's capabilities, 16 antennas were integrated into the second tank. Hereby, the antennas are spaced roughly 7.8 cm apart, or every 22.5°. Slots were milled with a Dremel Multitool and were roughly 1.5 x 70 mm so that the antennas would fit in with minimal margin. The antennas were inserted 8.5 mm out of the tank so that the insertion depth of 21.5 mm corresponded with the insertion depth in the first tank. At that depth, the antennas nicely resonated around 434 MHz. For an accurate alignment, a template was used for milling, see Figure 3.4a. Another template was used to align the antennas to the centre and two more to allow for glueing them in at the correct depth, see Figure 3.4b. The fabrication process was photographed in Figure 3.4c.

Antennas

There were 21 of the same type of antenna at our disposal. The antennas are of Yagi-Uda type, without a director plate. They are more commonly used within the department and are ordered externally. They are designed to resonate at 434 MHz in water, as that is the clinical HT frequency. A single antenna consists of a rectangular (70x32x1.52 mm) piece of dielectric material, with on either side an antenna arm of a thin metal layer, see Figure 3.5. These antenna arms are pointed to different sides to create a dipole antenna. On one side, a Balun (Balance-Unbalance) is incorporated, which is another rectangular piece of thin metal deposited on the dielectric. Hereby, the unbalanced signal from the feeder is transformed into a balanced signal for the antenna arms, as well as shifting the impedance to match the

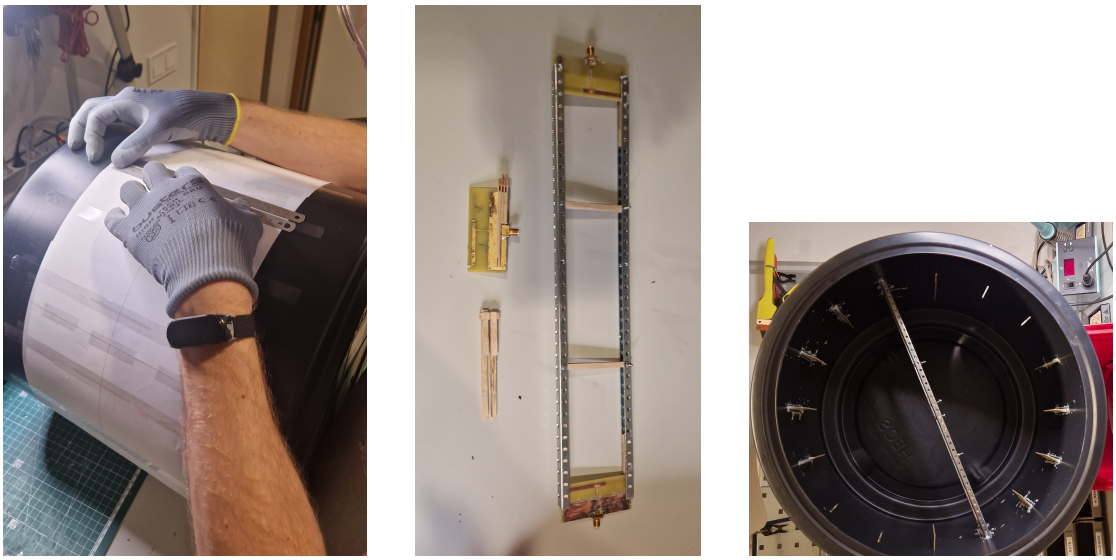

(a) (b) (c)

Figure 3.4: Assembly of Imaging Tank 2. (a): Tank with the template for the antenna slots. Additionally, two metal rulers were used to get the slots as straight as possible. (b): Internal alignment piece (right) and insertion depth templates (left). (c): Internal alignment template being used inside tank.

antenna's and allow for maximal radiating efficiency. The antennas have a SMA-F connector soldered on the backside. The full dimensions of the antennas can be found in Figure 3.6.

3.2 Software

MATLAB

To secure the synchronous switching to a new antenna combination in the switching matrix and a measurement execution by the VNA, various MATLAB scripts were used. The most relevant scripts can be found in Appendix B. The script calls several functions, which are named as straightforward as possible. If desired, the functions can be accessed via the GitHub repository. The following MATLAB toolboxes were used: Image Processing Toolbox, labelpoints, RF Toolbox, Instrument Control Toolbox, Instrument Control Toolbox Support Package for Rohde&Schwarz VISA Interface and the Navigation Toolbox. The employed MATLAB version was 2021b.

COMSOL

The simulation software COMSOL Multiphysics was used for the analysis of the initial electric fields in the imaging tanks. COMSOL is a finite element solver (FE) for physics problems. For our purpose, the Radio-frequency and Heat Transfer toolboxes were used in COMSOL 6.1.

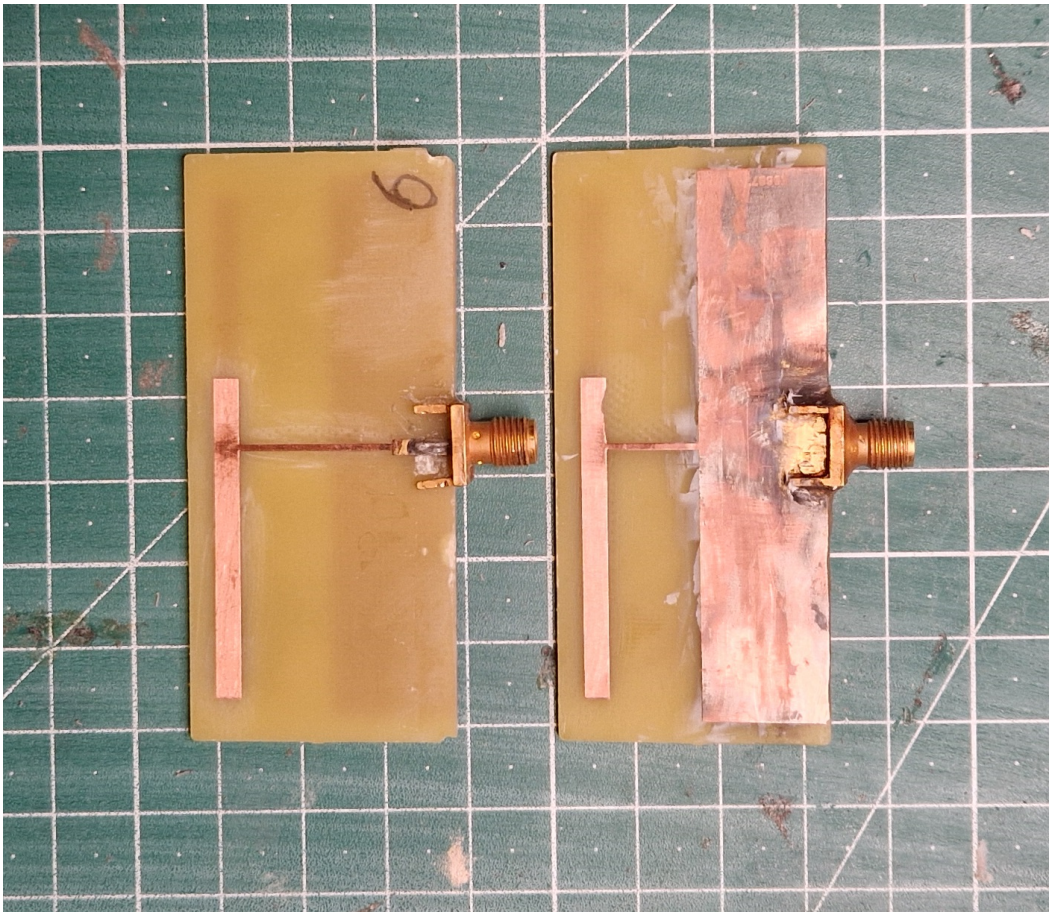

Figure 3.5: Image of two antennas, cleaned. One side with and one without the Balun plate.

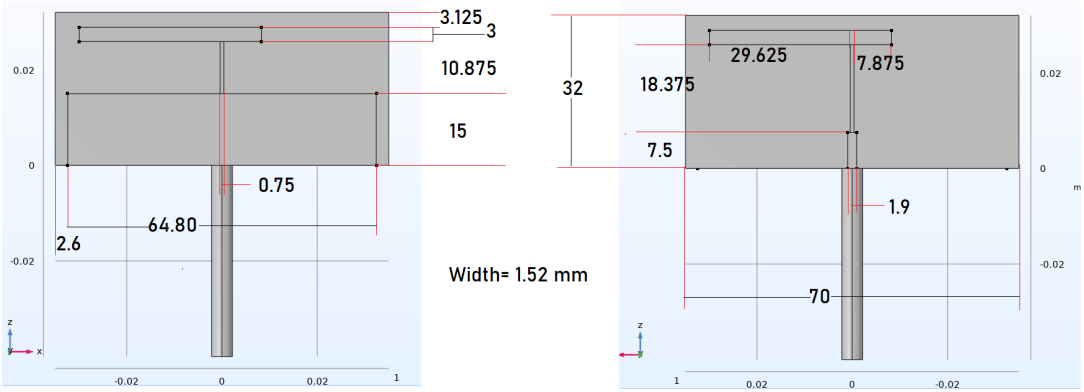

Figure 3.6: Antenna dimensions in mm. On the left, the side with the Balun. The coax cable on the bottom is of arbitrary length.

Servers

Most simulations and calculations could not be run on local computers or laptops. Therefore, some servers were utilised. The COMSOL calculations were executed with the computing power of the DelftBlue cluster and a server of the Applied Sciences Optics department, the latter of which was kindly made available. Both are based at the TU Delft. The Uluru system is alike the DelftBlue cluster and it is used by the Radiotherapy department. HTSERVER04 is a server of the Hyperthermia Unit. These two systems are based at the EMC.

- The DelftBlue cluster is a supercomputer operated by the Delft High-Performance Computing Centre (DHPC) that consists of a multitude of computational nodes, GPU nodes and high-memory nodes. Mostly, single computational nodes of type 1 were used. These are Intel Xeon nodes with 48 CPU cores and 192 GB RAM. For larger computations, computational nodes of type 2 were used. They also consist of Intel Xeon compute nodes, but then with 64 CPU cores and 256 GB RAM. On DelftBlue, users can send in jobs via a Linux-based system. Jobs are prioritised by a prioritising algorithm. When enough capacity is free, the job will run. This makes optimal use of the computer's capabilities but does not allow for visual interaction with the software. DelftBlue is not intended for large and sequential jobs, and unfortunately, COMSOL does not paralise well. Therefore, the prioritization was impacted negatively.
- The Optics department server holds 56 CPU cores and 256 GB RAM. It has the advantage of being a visual server over DelftBlue. This server was not always (wholly) available, as other users could access the server at the same time.
- The Uluru system at the RT department was used to execute reconstruction. This Linux system works with non-interactive shell jobs, alike DelftBlue. It is therefore much quicker than visual interfaces and servers. The Uluru system holds 30 nodes, of which a few are available for research. A normal node has 16 Intel E5-2690 cores and 128 GB RAM. For computations with a GPU, a node with either an NVIDIA A50, A1000, RTX8000 or RTX6000 was used.
- The hyperthermia server HTSERVER04 is a clinical server with 3 NVIDIA A10 GPUs, 256 GB RAM and 32 Intel Xeon Gold CPU cores. It is normally not intended for research, but an exemption was made for the final steps of this project.

Sim4Life

Furthermore, Sim4Life was used to model the first imaging tank and predict the EM field. Sim4Life is the clinically used treatment planning tool at EMC for deep hyperthermia treatments. It was developed by Zurich MedTech AG and the employed version was 7.4. Sim4Life less accurate than COMSOL, as it uses FDTD, and was therefore initially only used for validation. Steps to integrate it into the clinical pipeline will be described in the Discussion.

Reconstruction

The code for reconstruction was previously generated by Dr. Zanoli and run in MATLAB. Input files were generated with an additional set of MATLAB scripts, which extract a series

of parameters from the COMSOL simulations.

4. Methods

This chapter describes how different aspects of physical and computational research were conducted.

4.1 Switching Matrix characterization

Reverse engineering and testing

The SwMat was assembled elsewhere by other people than the ones working on the project. Unfortunately, this meant that the accompanying code to steer the SwMat had also been lost. Therefore, the relationship between the Arduino outputs and switch status had to be reverse-engineered. With a portable multimeter, the power over a switch could be detected. With lots of trial and error, the Arduino configurations for all 32 channels through the SwMat were found.

An Arduino script was developed to connect any two ports. To test whether the code could effectively connect all 120 combinations one after another, a test with LEDs was developed. Instead of the VNA, a DC power source was attached to the two output ports. At the antenna ports, 16 LEDs were inserted into the SMA-F connector, with a tiny ring of copper wire to ensure connection to the outer conductor. Subsequently, the code was run and the LEDs were filmed. The code connects the ports in ascending order, starting with 1+2, 1+3, 1+4 and ending at 15+16.

Switching times

The switches in the SwMat are mechanical. Thus, there is some time delay between sending the signals to the switches and the physical switching to the new connection. Moreover, each combination of switches requires the setting of 30+ digital outputs on the Arduino, which is again not instantaneous. Using Arduino's built-in $tic - toc$ function, the time of the sending of the digital signals could be retrieved. The physical switching time was measured by a series of delay measurements. After the MATLAB code had given the signal for the Arduino to switch, a delay was added before the VNA would start its sweep. The series describes the measurements with 0 (no signal), 0.1, 0,2, 0,25, 0.3, 0.6 and 0.9 seconds.

Signal leakage test

The SwMat consists of numerous wires and other electrical components. If a current runs through, an electric field will arise. It is, however, crucial that this field does not induce currents in other components. Thereby it can possibly disrupt the signal and lose power, so-called leaking. This signal "shortcut" is highly unwanted, as it could bury the signal going via the antennas and through the patient, which is what we are after. To this end, a leakage test was performed. The 16 antenna outputs were connected in eight pairs of two by the 1.5m coax cables. Subsequently, the normal 120-combination sweep was run over a frequency range of 100 MHz to 3 GHz with 291 samples. It was expected to see high transmission and low reflection only in the eight connected outputs. Some MATLAB code was developed to quickly analyse and plot these responses.

4.2 Simulations

COMSOL empty tank simulations

Models of the tanks were set up per COMSOL Multiphysics Server with MATLAB. This allows the user to run MATLAB code to generate the model and set up the solvers in a clear and overseeable way. General code for different applicators was previously made available by Dr. Zanoli per github/thermal-therapy/matlab-comsol. Starting from a template code, scripts were generated to correspond with the imaging tanks' dimensions and the correct antenna type. Subsequently, the simulation was run on either the Optics server or DelftBlue. COMSOL calculates the electric field and the loss in the tank that is filled with water, for all 18 or 16 ports radiating at 434 MHz and 1 W power. Calculation times, mesh element count and required computational resources were recorded. Imaging Tank 2 was reduced to 1/2 of its height to limit the size of the model and to suppress extensive computation times.

Another two simulations were executed to grasp the antenna response over a wider frequency range. This was done in order to compare the measured antenna response to the simulated one. A first, broader, frequency sweep simulated the E-field and loss for only antenna 1 at 341 till 527 MHz, for every 31 MHz. This yields a total of seven simulations. The S11 parameter is of specific interest, as that should correspond to the reflection measured by the VNA. A second, finer, frequency sweep simulated the response over the range of 404 to 464 MHz, in steps of 10 MHz.

COMSOL, as stated before, uses FEM to analyse the physical behaviour of the model. Thereby, it discretises the model into tiny elements by meshing. Special care was taken when setting up this mesh. In general, ten elements were placed per wavelength, with another factor five finer at the singularity points. These singularity points can be found at the sharp metal edges of the antenna arms, where the E-field changes drastically. Also, mesh elements end at the edge of objects such as the antennas and tank. On the outer part of the model, five identical square layers are placed. They are modelled to be perfectly matched layers, by which they emulate an infinite simulation domain. Thereby, the EM waves will eventually die out. This removes unwanted reflections at the edges of the simulation.

COMSOL phantom simulations

Another simulation was run with the inclusion of a phantom. This was of added value to grasp the E-Field and loss in the phantom, with scatter and heating in mind. The phantom model was based on a real phantom based in the lab. This phantom is a 12.5 cm diameter PVC pipe with a fat-like filling. Therefore, its relative permittivity and conductivity are 60.8 and 0.46 S/m, respectively. The phantom was simulated to be in the exact middle of the tank. An additional script was created to tweak the phantom to the user's preferences. Moreover, other scripts were edited to be compatible.

COMSOL and Sim4Life comparison

Whereas it is known that COMSOL is more accurate than Sim4Life, it was still desired to compare the simulated E-fields. Not only for comparison and validation but also with the target of disconnecting from COMSOL for clinical implementation. The Sim4Life model of Imaging Tank 1 was created using its model builder. The antenna array was created with a Python script, which would import and clone the antenna model, and translate each antenna into a circular orientation. Here again, the simulation was executed over all 18 antennas for a power of 1 W.

COMSOL antenna asymmetry

As the imaging tanks are both radially symmetric, rotary symmetry can be expected with respect to each antenna's response. To test if this is indeed the case, the extracted fields from COMSOL were compared in MATLAB. Only the axial slices at z = 0 m, the antenna height, were compared. There, the fields are the strongest and therefore most representative of the simulations.

4.3 De-embedding and calibration

The switching matrix allows us to make a collection of 120 2-port networks readily available for measurements by the VNA. In the imaging measurement, it is placed before (and technically also after) the imaging tank as a cascade network. It thereby also has a characteristic S-matrix, which will disrupt the output S-matrix acquired by the imaging from the S-matrix of the object and tank itself.

The latter is the one we are mainly interested in for our inversion. Thus, we need to remove the influence of S_{SwMat} from the total measurement of S_{tot} to retrieve S_{tank}. The latter depicts the characterisation of the scattering in the tank. S_{tank} thus also corresponds to S_{sca}. We can do so by first fully characterizing S_{SwMat}, like a calibration. Note that not only the SwMat but also the VNA-SwMat cable and SwMat-tank cable are part of the S_{SwMat} component we consider. In Figure 4.1, a schematic depiction can be found.

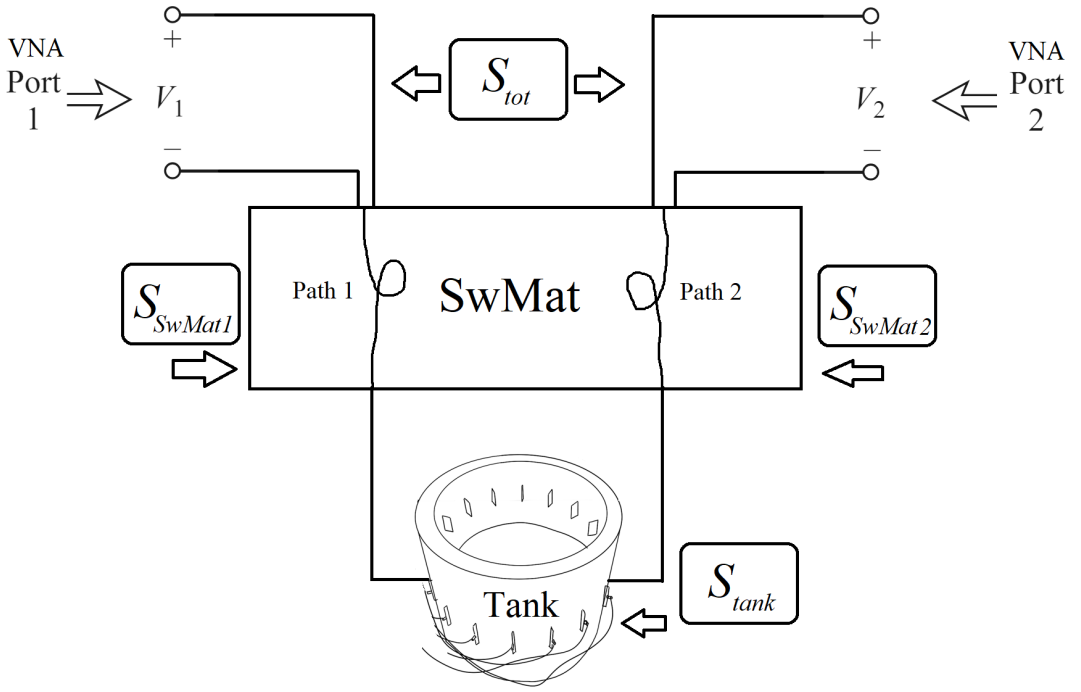

Figure 4.1: Depiction of a two-port network as it measures an antenna combination via the SwMat. Observe that the SwMat poses a cascading of two S matrices, as S_{SwMat1} comes before and S_{SwMat2} comes after S_{tank}. Together, they yield S_{tot} as observed by the VNA.

We could go about retrieving data on S_{SwMat1} and S_{SwMat2} in several ways, which are mentioned in order of decreasing accuracy but thereby also decreasing complexity and effort:

1. Do a full OSMT(Open, short, match, through) calibration for each port combination.
2. Measure for all 2x16 ports a 2x2 S-matrix for a complete signal looped back into the VNA, for both paths through it.
3. Doing one OSM measurement and calibration for each path.
4. Attaching the same impedance match at the end of every path and measuring the reflection.

It was decided to go about with method two, as it is way less cumbersome than method one. Also, it is more accurate than methods three and four as they do not allow for calibration of the S21 and S12 parameters. In all cases, it is important to use the same cable connections as in the eventual imaging measurements. If done well, this measurement only needs to be executed once and the de-embedding can then be done with the same S_{SwMat} ever after. In this setup, the calibration happens at the ends of the VNA-SwMat cables, so these are also the calibration endpoints for all measurements to follow.

Here, we also touch upon calibration. To the disposal of this research were a Rohde&Schwarz

N-type Calibration kit and a KSMART SMA-type Calibration Kit. Calibration is crucial in shifting the reference plane and is therefore closely involved with de-embedding, which holds the same functionality.

The de-embedding method and script were tested by doing a direct and a through-matrix measurement, which could be compared. For the direct measurement, eight pairs of two antennas were characterised. From the through-matrix measurement, these same antenna pairs were extracted and de-embedded. More information on all measurements can be found in the next section.

4.4 Measurements

Different types of measurements were conducted, all with their own MATLAB script for automatisation. Measurements were conducted from a local computer, that steered both VNA and SwMat and retrieved the measurement values immediately. Before each measurement, the VNA was calibrated at the required reference plane. All cables were labelled and used consistently in the same place to isolate imperfections.

We distinguish the following measurements:

- Through-matrix measurement. This concerns a normal measurement with the imaging tank. Two cables connect the VNA to the SwMat input and 16 more connect the SwMat to the antennas in the imaging tank. For Imaging Tank 1, the two skipped antennas were recorded. As the measurement is executed, the SwMat is steered to connect a new combination of antennas, after which the VNA is triggered to do a sweep. The resulting values are collected and stored in two big S-matrices, with 16x16 (frequency points) entries. One matrix concerned all transmission measurements, the other all reflection measurements. To match all other antennas in a measurement, the unused antenna paths are passed to the SP8T switches, as they are properly terminated. Forgoing this would yield extra reflection of the unused antennas, and would also not correspond with the simulations. A photo of the setup can be seen in Figure 4.2.
- De-embed measurement. This measurement is meant to gather the characteristic response of all 32 paths through the matrix, with the purpose of using these later for de-embedding. All 16 cables are attached to the antenna ports of the VNA. First, only the cable from the first port of the VNA to the first port of the SwMat is connected, and an N-SMA adapter is placed on VNA port 2. Calibration is conducted at the adapter and port 1 cable end. The measurement then consists of connecting all 16 output cables back to the VNA, one after another and measuring the responses. Once finished, the process is repeated but now VNA port 2 is connected to the second port of the SwMat. The system is recalibrated in between. So, the other 16 paths can be characterized.
- Direct measurement. To verify the integrity of the de-embedding methodology, a comparison had to be made to a ground truth reading. For that, a direct measurement can be used. A series of antenna pairs can be picked to be involved in this. The VNA is hooked up with both cables and is calibrated at the cable's ends with the SMA calibration kit. Then, the first combination of antennas is connected and measured. All other ports

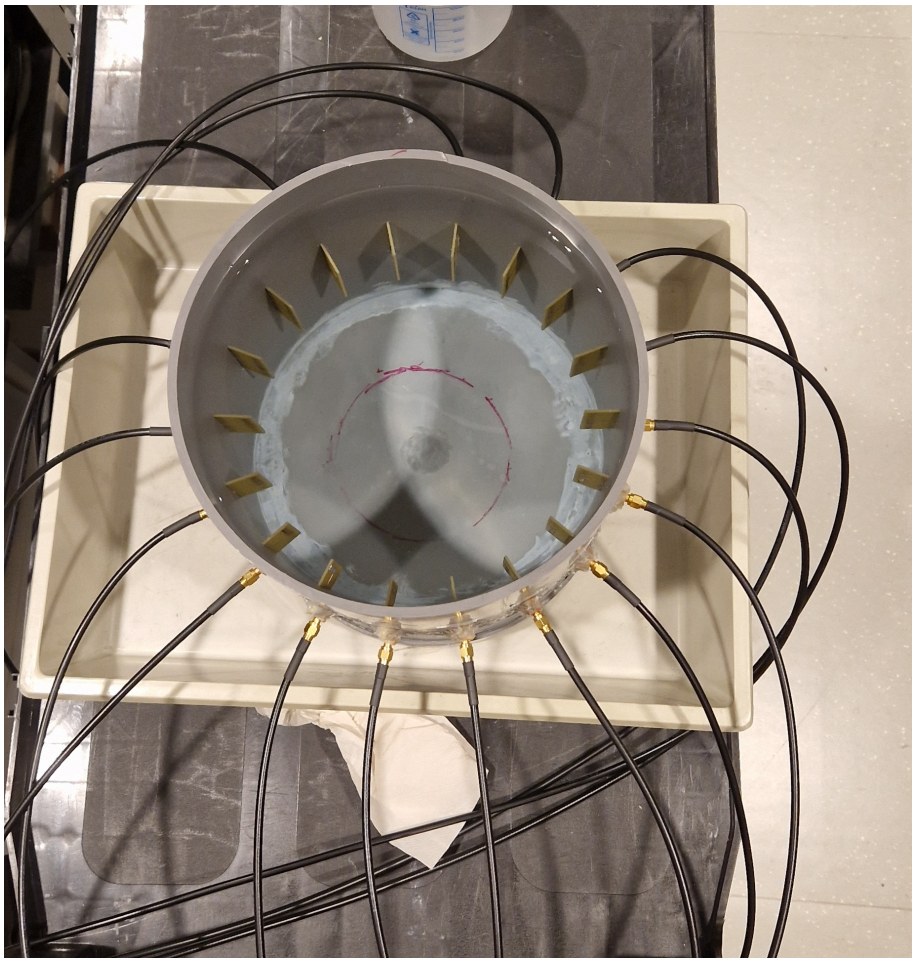

Figure 4.2: Top view of a measurement setup of a measurement with Imaging Tank 1. The first and third antenna counterclockwise from 12 o'clock are not connected with a cable, but terminated with a 50 Ohm match.

are matched with a 50 Ohm impedance. Then, the cables are disconnected, impedances are screwed on and the next combination is measured.

The code for all types of measurements can be found in Appendix B. The code for de-embed and direct measurement only entails the part that is different from the through-matrix measurement. The full code, functions and Arduino code can be found on the Git repository `thermal-therapy/switching-matrix`.

4.5 Reconstruction

Reconstruction approach

The background of the reconstruction method was introduced in Ill-posed Inversion in the Theory chapter. The goal of the inversion is to reconstruct the contrast distribution as well as the total electric field. The inversion algorithm makes use of a stabilized bi-conjugate gradient to evaluate the update steps and adjoint formulation to evaluate the Jacobian of the cost

function. Furthermore, instead of evaluating the convolution per Green's function, a Fast Fourier Transform (FFT) is used. The discrete kernel $\boldsymbol{g}$ following from Green's function G can be stated as

$$\boldsymbol{g} = \mathscr{K}\{G\}, \tag{4.1}$$

with $\mathscr{K}$ being a function that discretises and sums G over the elements created. Hereby, the scattered field can be depicted as

$$\mathbf{E}_{\text{sca}} = \mathscr{F}^{-1}[\mathscr{F}\{\boldsymbol{g}\}\mathscr{F}\{\chi\mathbf{E}_{\text{tot}}\}], \tag{4.2}$$

where $\mathscr{F}$ and $\mathscr{F}^{-1}$ depict the forward and inverse FFT, respectively. We also find that $\mathbf{E}_{\text{inc}}$ can be written as a function of $\mathbf{E}_{\text{tot}}$ in matrix formulation per

$$\mathcal{F}(\mathbf{E}_{\text{tot}}) = \mathbf{A}\mathbf{E}_{\text{tot}} = \mathbf{E}_{\text{tot}} - \mathbf{M}\chi\mathbf{E}_{\text{tot}} = \mathbf{E}_{\text{inc}}. \tag{4.3}$$

Note that A in equation (4.3) is a matrix encapsulating the function $\mathcal{F}$ and that this equation holds for each radiating antenna.

We can use this formulation to calculate gradients (derivatives) to numerous variables, yet we are mostly interested in the derivatives to the contrast χ and total electric field $\mathbf{E}_{\text{tot}}$. The adjoint formulation proves to be a simpler way of computing multiple gradients. It uses one intermediate step to set the functional (nominator) of the derivative, after which it allows for the gradients to various parameters (denominators) to be calculated efficiently. Since the matrices are quite extensive, this saves a lot of time and computation power.

The full inversion scheme is pending patent approval and can therefore not be disclosed here.

Synthetic data

Reconstruction with synthetic data was attempted at the Uluru system but ultimately failed. It was possible to conduct a test run on HTSERVER04. The data was extracted for a COMSOL model with a patient model as the object.

Acquired data

Unfortunately, full reconstruction from measured data to an image of EPs proved a bridge too far for the span of this project. However, code was made to manipulate the measurement so that it would be ready to run in the reconstruction script. This was especially needed for Imaging Tank 1, for which the model simulated more antennas than were measured. Those entries had to be removed for correspondence. Also, only the measurement at 434 MHz should be taken, yielingd only a single 16x16 S-matrix.

5. Results

5.1 Switching Matrix characterization

Reverse engineering and testing

The generated code to run through all 120 combinations was found to be successful. A (sped up) movie of the LED test can be found online, as supplementary video S1. This video can be accessed via `https://drive.google.com/drive/folders/18wxjfxAKQNuG_6qUJ4tcDlxM5R9wsqIK?usp=drive_link`. As can be seen in the video, the ports are connected in the correct ascending order. Port 1, on the top left, is first connected with port 2, on the bottom left. Consequently, all other ports are connected until port 16, at the bottom right. Then, port 2 becomes the first port, etc. Some LEDs might show up brighter light than others. It was found that this can be due to the LED themselves differing, but also because of a tighter or looser connection with the copper wire ring to the connector. Since the LEDs did light up in the right order, the code was accepted as correct. Possible leakage of power was not yet considered here, but it was later investigated in the experiments for Signal leakage test.

Switching times

Regarding the delay times of 0, 0.1, 0,2, 0,25, 0.3, 0.6 and 0.9 seconds, it was expected that the lower values would show faulty measurements. The physical connections would not yet be completed as the VNA would have started measuring. However, once the physical switching has passed, so for larger delays, the measurements would look similar and correct. The results can be found in Figure 5.1. The VNA measures the frequency from low to high, so left to right. In the plots, every tenth sample from the 101 measurement point is indicated with a time marker. It can be seen that for 0 and 0.1 seconds delay, the transmission hovers around the noise threshold of -120 dB and the reflection is high at 0 dB. For all the other delays, the transmission is high and the reflection shows a characteristic response, with some resonance frequencies. These resonances are likely due to the components of the SwMat. Note that at the end of the 0.1 delay sweep, the S12 parameter goes up and the S11 goes down. This might indicate that by the end of this sweep, the physical connection had just been made. From these results, it was concluded that a 0.2-second delay was enough for adequate measurements. It was therefore used as the standard delay for the rest of the measurements.

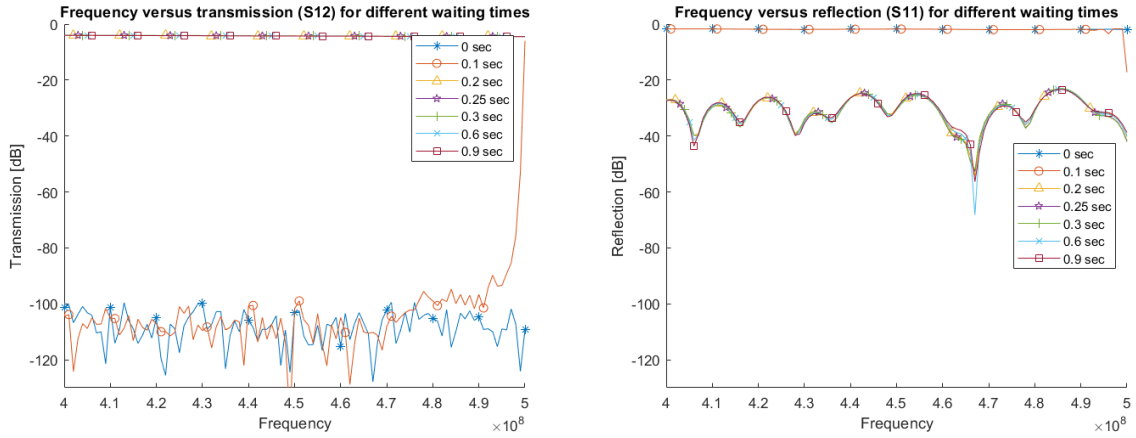

(a) (b)

Figure 5.1: Response versus frequency over a series of delays. (a): Transmission response. (b): Reflection response

Signal leakage test

A series of combinations of connected antenna ports were tested. For 1+16, 2+15 ... 8+9, the results of two of these tests can be found in 5.2. Both average transmission and average reflection are reported. Measurements are depicted as a ratio of 1, which depicts the amplitude of the incident wave. The code would automatically label reflections under 0.5 and transmissions over 0.5. It was expected to see eight peaks in the transmission measurements and eight valleys in the reflection measurements. As can be seen in the first row, seven combinations show low reflection and high transmission. However, valleys are also abundant around 0.5. These measurements correspond with combinations involving port 11 as the second port. There, an unusual reflection takes place, as port 6 and port 11 should be connected. The transmission of that very port combination is also lower, as it is around 0.45, whereas the others are around 0.75. From this, it was found that something was off in the second-port path to antenna 11. In the second row, we find this issue resolved. This measurement was taken after the odd-number rotary switch at the second port was replaced. This was identified to be causing the problems with port 11.

5.2 Simulations

COMSOL empty tank simulations

The calculated electric field strength and the loss in imaging tank 1 can be found in Figures 5.3a and 5.3b. Portrayed is the axial slice at z = 0 m, where the antennas have their midpoint. In the simulation snapshot, port 1 is radiating, and all the other ports are simulated to be perfectly matched. The simulation for Imaging Tank 2, port 1, can be found in Figures 5.3c and 5.3d.

To elucidate the mesh generation and element distribution of the tank models, Figure 5.4

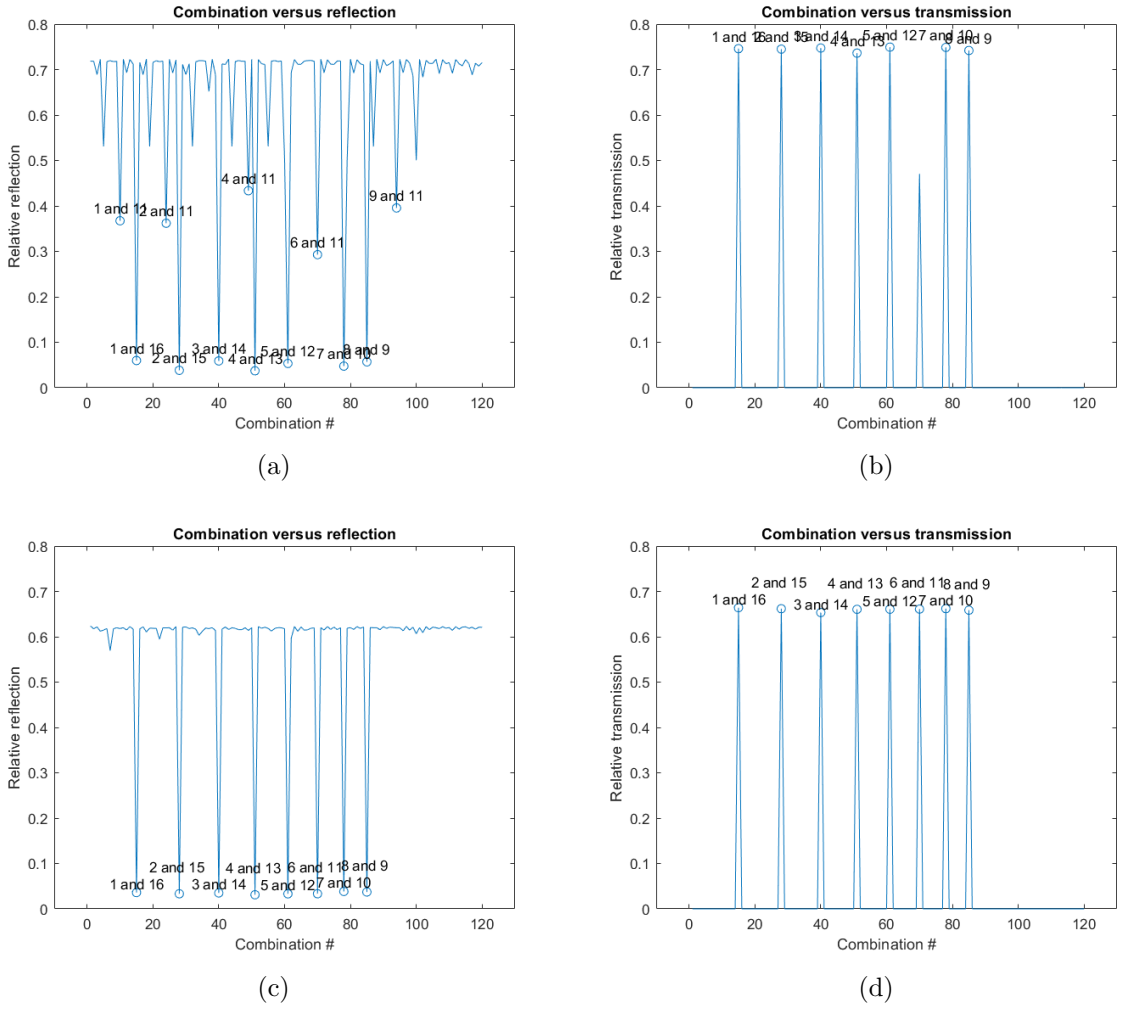

Figure 5.2: Average relative reflection and transmission over 120 combinations. (a): reflection with faulty path. (b): transmission with faulty path. (c): reflection with working paths. (d): transmission with working paths.

shows an axial cut of the mesh at z = 0 m for Imaging Tank 2's model. From here, it can be seen that the antennas and tank are especially finely meshed. the further out, the more coarsely the mesh becomes. Finally, the rectangular elements concern the perfectly matched layers.

In Table 5.1, an overview of mesh element, computation time and file size are reported for different simulations. It can be found that for Imaging Tank 2, the normal DelftBlue nodes are not sufficient. Whereas the increase in (un)solved file size is not a direct reason for concern, it does appear that the roughly 50% increase in element count is a heavy burden on the computation. This is also reflected by the time it takes to solve, as the 33 minutes to 5 hours and 13 minutes is more than a 9-fold increase. We can explain this increase by the internal memory capacity of COMSOL. There is a cap on the in-core, faster, solver's memory around 48 GB (a quarter of the total RAM). Upon reaching this limit, COMSOL will start writing temporary files to store the calculations, which is naturally slower. Only the solving of Imaging Tank 2 overrides the capacity. Note that for the full model of this tank, the computation time

Simulation	Size (unsol)	Size (sol)	Comp time	Elements	Server
Tank 1 empty	64.9 MB	3.88 GB	33 min	1.17 mln	Optics/DBlue comp1
Tank 1 + phantom	67.6 MB	4.07 GB	38 min	1.22 mln	DBlue comp1
Tank 1 freq sweep	65.4 MB	4.99 GB	1 h 45 min	1.17 mln	DBlue comp1
Tank 2 (1/2)	86.2 MB	6.24 GB	5 h 13 min	1.87 mln	DBlue comp2

Table 5.1: Table with Simulation description, model file size unsolved (unsol), model file size solved (sol), computation time (comp), mesh element count, and server type used. DBlue = Delft Blue Cluster, comp1 = computational node type 1, comp2 = computational node type 2.

would be enormous. On the first type of DelftBlue node, the memory limit causes an error, as the temporary files cannot be read and/or written simultaneously within the system's capacity. Therefore, it bugs out, indicating that the solver could not converge. Thus, this calculation was done on a type-2 node.

COMSOL phantom simulations

The axial slices at z = 0 m of the phantom simulation are provided in Figure 5.5. Noticeable is the high loss just inside the phantom, close to the radiating antenna. Furthermore, the E-field behind the phantom is much less strong than before, recall Figure 5.3a. Also, the phantom seems to scatter the field a bit, as the values close to the antenna are more equal. The high loss inside the phantom was expected, despite the lower E-field value at the same location. Mainly, the phantom's conductivity of 0.46 S/m is way higher than that of deionized water with 5.5 μS/m.

COMSOL and Sim4Life comparison

In Figure 5.6, images of the Sim4Life simulation can be found. This simulation, for all 18 antennas in Imaging Tank 1, took about 2 hours. Though the scaling is different, the similarity to the fields in Figure 5.3 (top row) can be observed. Thereby, we can verify the correctness. Also, the lower resolution can be retrieved, especially in Figure 5.6a as opposed to Figure 5.3a.

Rotary symmetry

The extracted fields are discretised as voxel averages. Therefore, the finely meshed model is reduced to 50-100 voxels in each dimension. This is sufficient and necessary for further processing. For Imaging Tank 1, we can compare only directly opposing antennas, because of the described discretisation. Figure 5.7 shows the percentage difference of two opposing antennas' field norms. These plots were acquired by rotating the second antenna's field 180°, taking the absolute difference and dividing it by the first field. As can be seen, the fields largely correspond within the domain. On average, the difference is <1%. As can be seen in Figure 5.3a, the field strength is highly different within the tank. As the difference-heatmaps do not show this heterogeneity, it is deduced that radial symmetry surely exists. What does appear quite clearly in all comparisons, is a circular pattern with about 18 dots. These differences were found to overlap with the antenna locations.

Both the large differences at the antenna points and the non-perfect equality of the fields within the domain are attributed to the spatial sampling rate of the MATLAB code. This may cause just some mesh elements to contribute to another pixel in the comparison, which can yield the offset.

5.3 Measurements and de-embedding

To compare the simulated response with the measured data, we simulated a frequency sweep. Frequency sweeps for only antenna 1 at 341 till 527 MHz, for every 31 MHz, plus 404 to 464 MHz, in steps of 10 MHz, were conducted. A corresponding direct measurement was done, and all antenna reflection responses were averaged. The overlay can be found in Figure 5.8. Here, it can be observed that the traces are of similar shape, and the resonance frequency is about the same at 424 MHz. Also, there is still enough resonance ($<$10 dB reflection) at our target frequency of 434 MHz. However, it can also be seen that the amplitude is somewhat different. Overall, the model predicts more reflection than reality. It is not clear why the simulation counts on more reflection, but it can be a consequence of the simplified connectors and antenna model. Also, it could be that in reality, more signal is "lost", which yields neither transmission nor reflection. Possibly, the model does not take that factor into account, yielding a higher reflection. However, this comparison does elucidate that the antenna model is sufficient, and that the predicted fields are usable.

To assess the correctness of the de-embedding methods, Figure 5.9 gives an overview of the effect. Because we compare to a ground truth of a direct measurement, we can only depict two antennas. In this case, that would be #3 and #4. We can see in Figure 5.9a that the de-embedding works very well for lower and higher frequencies, as the direct (blue) and de-embedded (red) measurements almost overlap, as opposed to the matrix measurement (green). For the middle frequencies of the range, the overlap can not be observed as much, though the resonance frequency seems to be more similar to ground truth. For the phase, as depicted in 5.9b, it can be seen again that the ground truth signal is correctly restored. The reflection in antenna #3, S11, also seems to follow a good trend, but it is not entirely correct. However, it can be seen that the de-embedding restores the signal to what it is supposed to be. It is important to mention that for other antenna pairs, the quality of de-embedding could differ. Overall, the method seemed to work properly, yet deviations were unavoidable. This could be due to flawed measurements. Due to the considerable amount of time it takes to perform one of these measurements, the experiment could not be repeated. However, an earlier test using Imaging Tank 1 already proved that de-embedding worked for reflection very well. The needed calibration kit was unavailable at the time of that measurement, explaining the poorer performance for transmission. An overview of these results can be found in Appendix C. The measurements of the paths themselves are visually assessed before continuing. One de-embedding measurement is depicted in Appendix D for all 16 paths through ports A and B, respectively.

5.4 Reconstruction

One reconstruction with synthetic data from Sim4Life was successfully run several times on the HTSERVER04. It took roughly 30 minutes for 15 iterations to converge to a solution. The results can be seen in 5.10a. Depicted are the simulated relative permittivity (EPS) and conductivity (SIG) at an axial slice of a patient's head model on the top row, followed by the reconstructed distributions on the bottom row. The slice is located around the mouth and the nose is pointing north. Immediately, it is clear that the reconstruction is blurred and cannot reach the original resolution. However, the contours are clearly visible and the values of the EPs come within a reasonable range. The regions of lower conductivity and permittivity are retrievable. In 5.10b, the convergence can be found according to the cost function. Especially in the conductivity, it can be seen that the contour is somewhat smaller. This is likely due to the smoothing of the reconstructions in all dimensions, also z, which is not observable in this 2D plot. However, as the head narrows under the jaw towards the neck, it can be expected that lower values occur there due to the air.

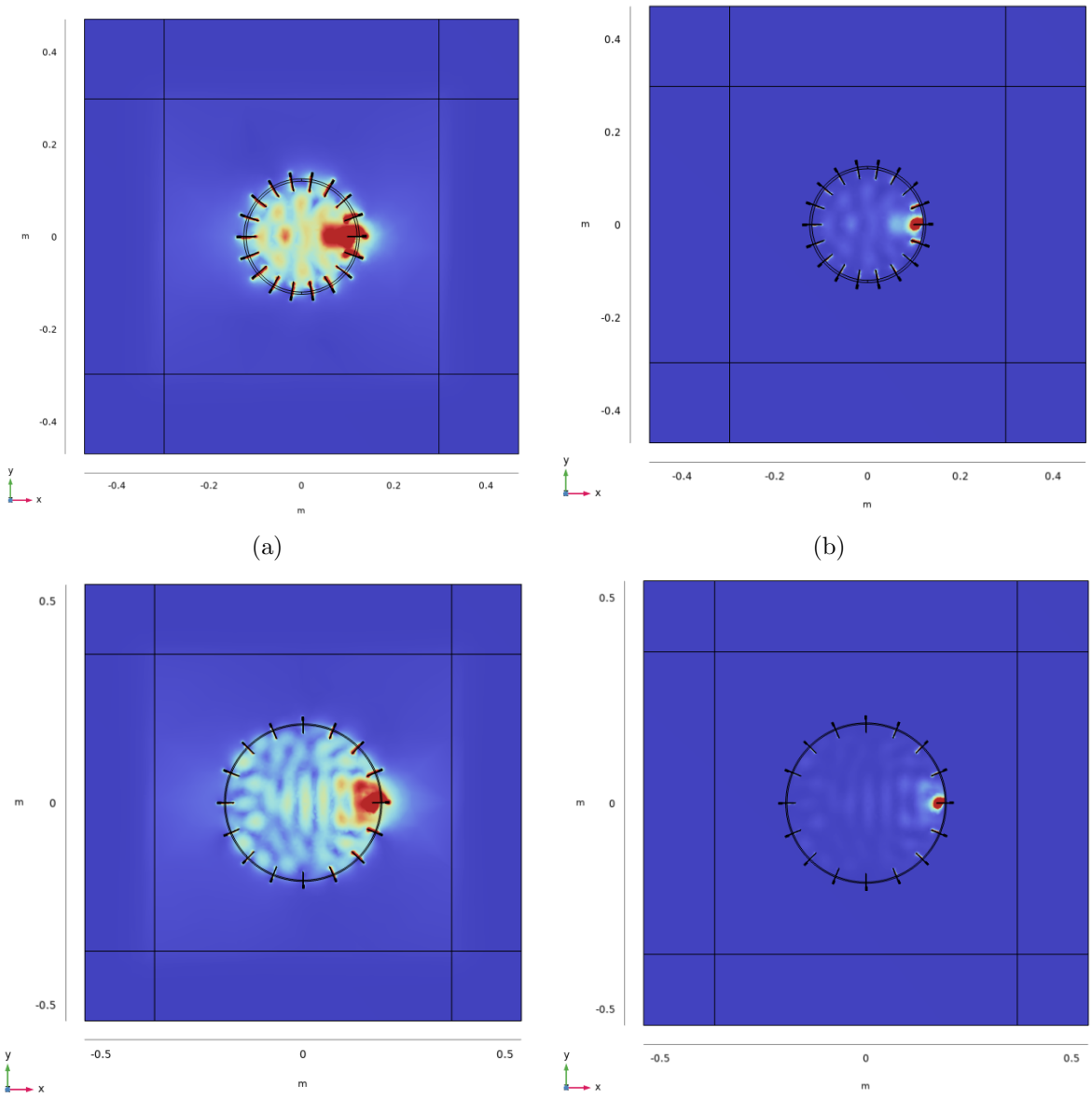

Figure 5.3: Electric field norms and losses for the two imaging tanks, as simulated by COMSOL (a): Tank 1, Field. (b): Tank 1, Loss. (c): Tank 2, Field. (d): Tank 2, Loss.

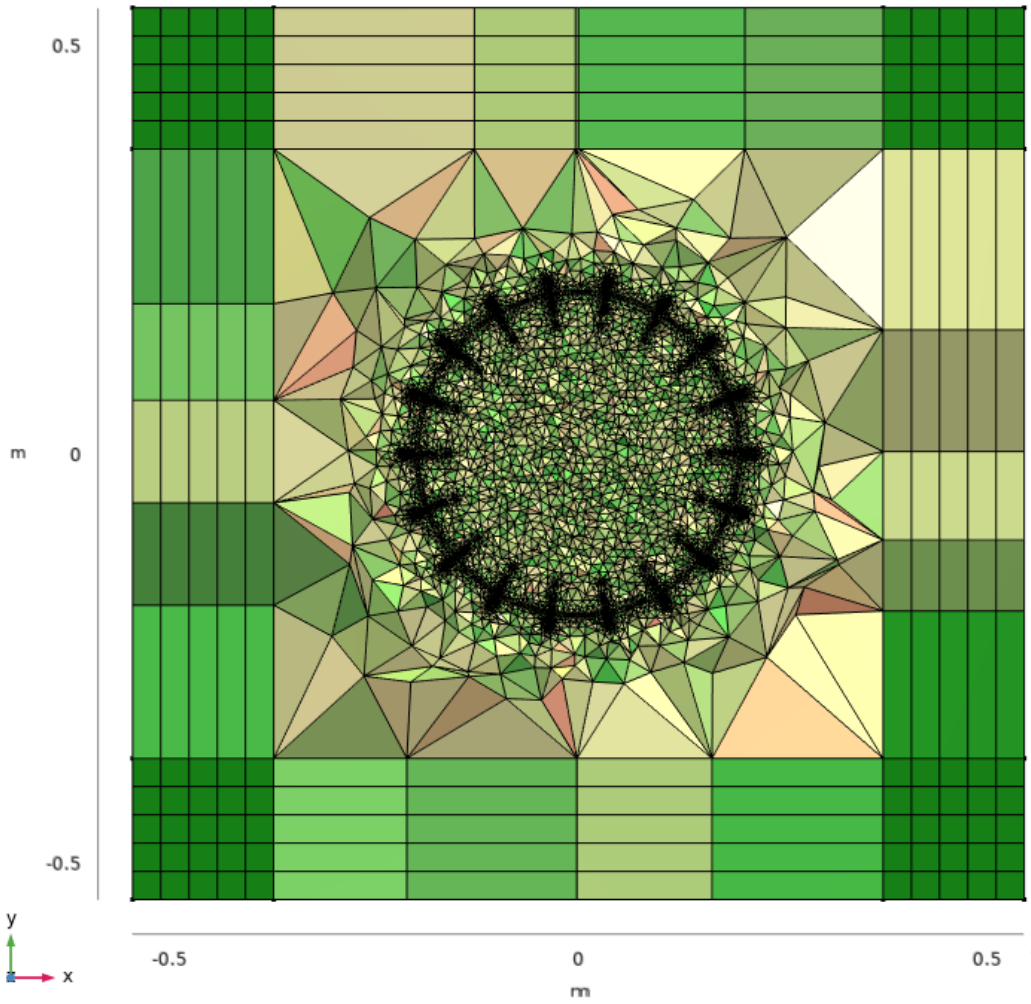

Figure 5.4: Mesh elements in COMSOL for an axial cut at z=0 for Imaging Tank 2. Different colour shades indicate how tilted an element's surface is with respect to the XY-plane.

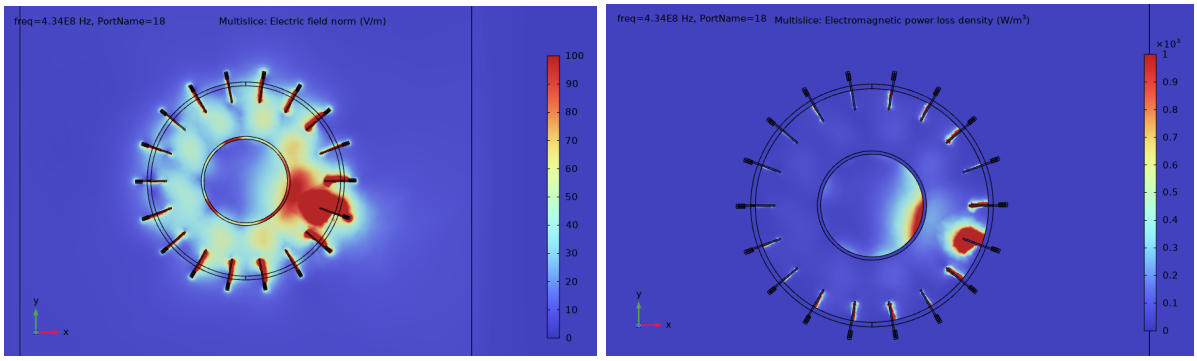

(a) (b)

Figure 5.5: Simulations with phantom result. (a) Electric field norm (V/m). (b) Loss ($W/m^{(3)}$).

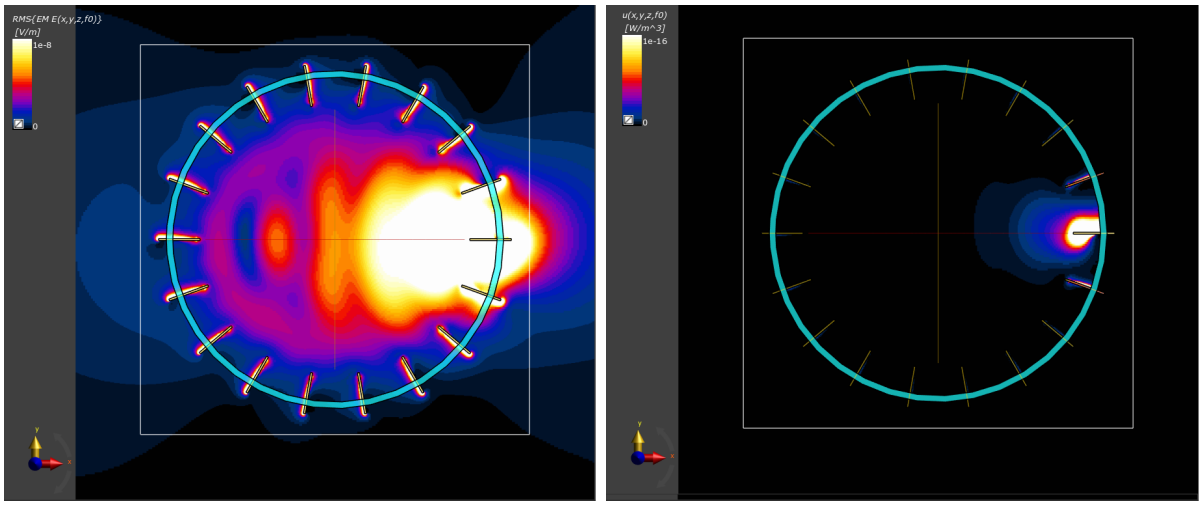

(a) (b)

Figure 5.6: Electric field norm and loss for Imaging tank 1, as simulated by Sim4Life (a): Electric Field norm (V/m). (b): Loss (W/m^3)

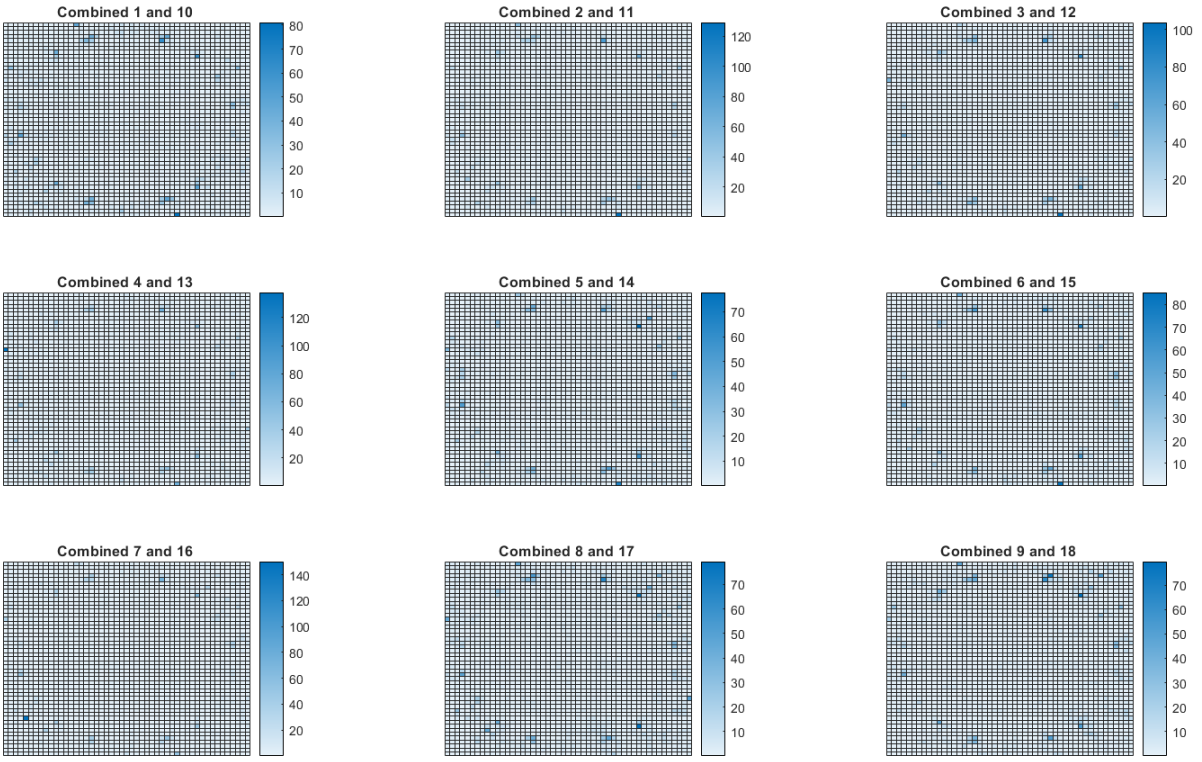

Figure 5.7: Rotational symmetry analysed as the percentage difference of two antenna fields. The antenna pairs always oppose each other.

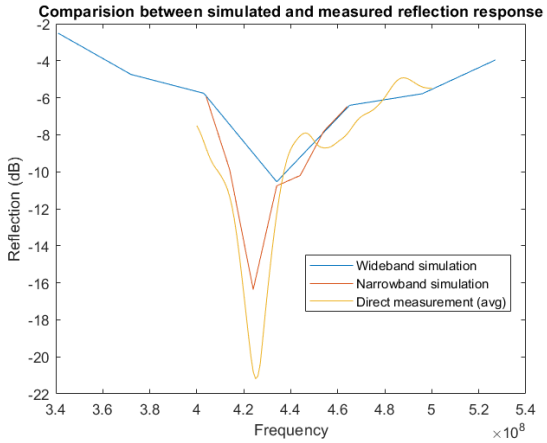

Figure 5.8: Simulated and measured antenna reflection values.

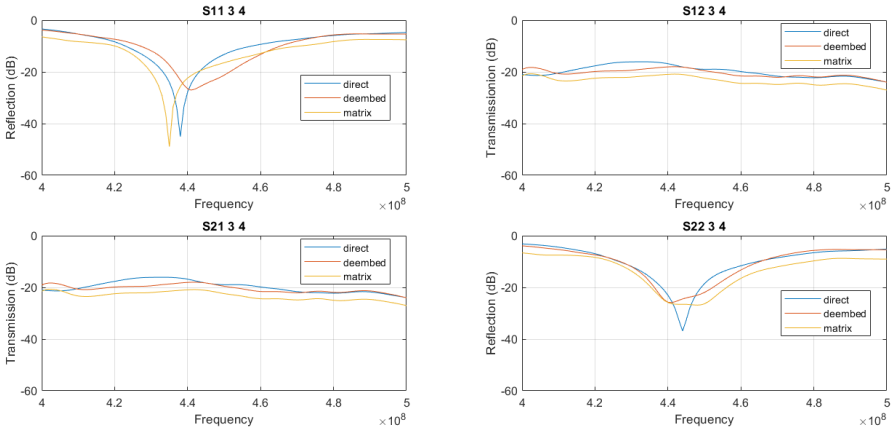

(a)

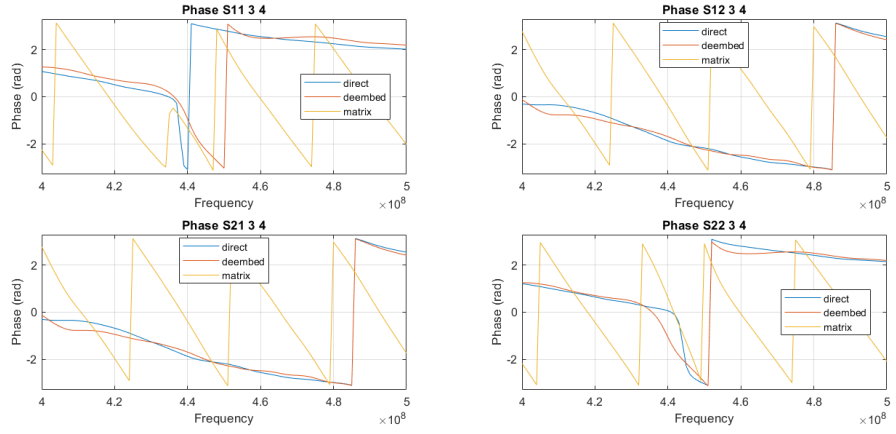

(b)

Figure 5.9: Comparison of direct, de-embedded matrix and through-matrix measurements for antennas #3 and #4 of Imaging Tank 2. (a): Magnitude versus frequency for all four S-parameters. (b) Phase versus frequency for all four S-parameters.

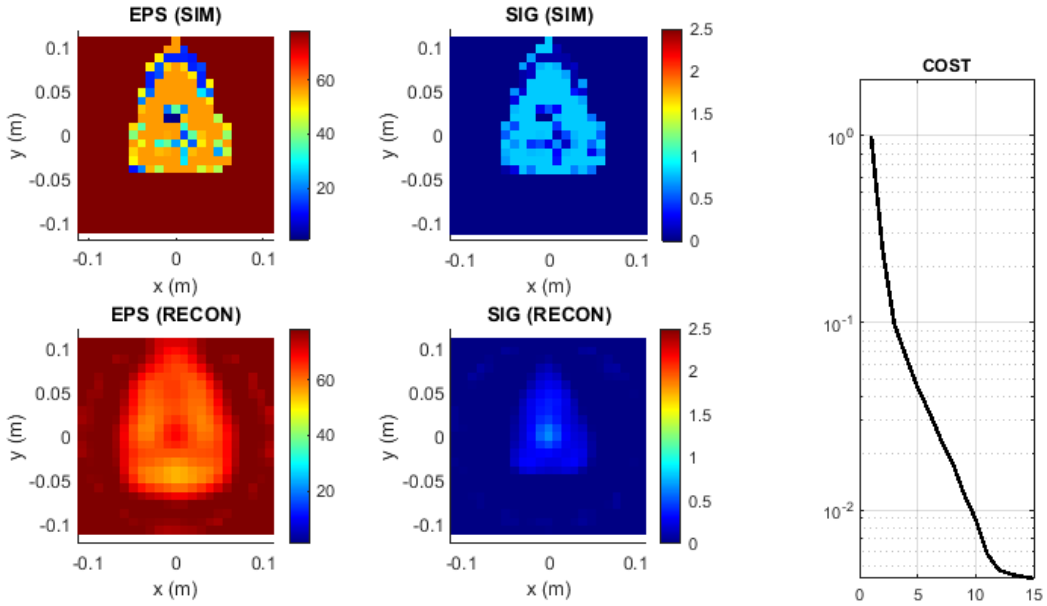

(a) (b)

Figure 5.10: Electric field norms and losses for the two imaging tanks, as simulated by COMSOL (a): Reconstruction of permittivity (left) and conductivity (right), where the top row depicts the reconstructed distribution and the bottom row the ground truth. (b) Cost function versus iteration step.

Discussion

Currently, hyperthermia treatments are limited in number, despite their ability to drastically increase clinical output for cancer patients. Due to limited accuracy and reproducibility, the modality has not taken off yet. The uncertainties regarding permittivity, conductivity within a patient, as well as patient positioning, can be improved with microwave tomography. Therefore, a dual-modality applicator, hardware and pipeline have to be realised. This research is the first step in that.

The proposed methodology proves that the integration of MT into an HT applicator is technically feasible. On the software side, progress still has to be made to come to a full pipeline. This is already the focus of ongoing research.

The switching matrix was tested and improved, which allows for automated and fast measurement of the S-matrix. The influence of the matrix can be removed via the proposed de-embedding methodology. COMSOL was used to accurately predict the response of the antennas in the imaging tanks and could be used to acquire the necessary files for the reconstruction of an image of the permittivity and conductivity distribution. Lastly, a reconstruction could be run with synthetic data.

The presented results for the simulations, unfortunately, cannot tell the complete story. For example, no attention was given to external influences on the EM fields. Metal objects near the imaging tank, or even just near a single antenna, could potentially disrupt a measurement, more specifically the reflection. This is an inherent limitation of the COMSOL models. It was found that the model prediction on the antenna's behaviour corresponds with the measured data, but it was not perfect. However, it is hard to generate a fully accurate model. The time needed to develop that would not be worth it, and you also lose some flexibility in the development of your tank.

Other limitations include the use of older hardware in the Switching Matrix. One switch already failed and had to be replaced. It is not unthinkable that other parts will follow, as the components have been refurbished several times. Also, when in use, one could hear the power of the fan decreasing as too many switches needed to be supplied with power. This could potentially impact the performance of the switches, though that was not seen up to this point.

As a recommendation, the author has made a list of improvements to the SwMat in the generated manual for the SwMat. With that manual, the SwMat could be used to other ends. These improvements include the incorporation of a second Arduino, which would make the

switching way less cumbersome. Instead of the 30+ outputs needed to be set now on every combination of ports, this could be reduced to a mere two or four. Though the Arduino itself is relatively fast, this would yield a smaller time delay needed. Setting fewer outputs means shortened signalling time, and by optimising the switching pattern, the physical switching time would also be reduced.

The time it takes to complete a full measurement is reasonable but can be shortened without adjusting the SwMat. For example by taking a smaller bandwidth. This would impact the possibility to redo measurements automatically. Ultimately, the physical switching in the SwMat is the limiting factor. As the VNA can measure a single frequency in an instant, switching through all 120 combinations would be the final threshold. It was found that around 0.2 seconds of delay would be enough, yielding a theoretical full-measurement time of less than 30 seconds.

Though a measurement rate of half a minute would be preferable for the continuation of HT without losing too much heat (temperature) in the patient, it requires extensive testing and validation of the measurement hardware, especially the SwMat, to be held up. The faster the measurement is, the less time and possibilities there are to check for errors. Eventually, the reconstruction will always take longer, so real-time visualisation is unachievable. However, we can strive for near-real-time visualisation for control purposes.

Moreover, the server capacity at the Hyperthermia Unit might cause issues when extensive reconstructions need to take place. Especially since more research and also important clinical processes run on these servers. Therefore, the Uluru system might be a good alternative, but special care should be taken to convert the code to a Linux-friendly version. The current, Windows-based, version is deemed incompatible. The Uluru system has more than enough capacity and could be integrated nicely into a pipeline with its remote job listing.

Besides this, the time and size of COMSOL simulations could become an issue. Even at the DelftBlue server, calculations could take several hours and grow up to GBs in (temporary) files. In the end, this is reduced to 1.5 GB of input files for the reconstruction. It is advised to further research the possibilities of using Sim4Life-based data for the reconstruction. Even more so because the EMC has no COMSOL license, making the simulation not durable. The good news is that when an applicator is realised, the simulation has to be run only once.

If it is decided to stick with COMSOL, it could be worthwhile to look at ways to improve the speed of computations. One could, for example, look at decreasing the amount of calculation. By exploiting the radial symmetry, fewer ports would have to be simulated. Also, the meshing could be made coarser further from the antennas and away from the centre, especially for bigger tanks, as the signal is more far-field-like over there. For example, a distance function based on the wavelength and tank height or radius would be a viable option for this.

For the integration of Sim4Life, it should be explored how accurate the simulated fields are with respect to COMSOL on a quantitative basis. With the discretisation in mind, it might be that for the middle of the tank, the simulation is just fine. Near the antennas, however, it might be less accurate. We already observed that this was not perfect for COMSOL. As the coupling and cross-talk between antennas is an unwanted but crucial to consider behaviour, it

is necessary to grasp it accurately. Furthermore, alike COMSOL, a simulation of a definitive applicator would only be necessary once. A good aspect of Sim4Life is that it would allow for more research and functionalities within the department's resources. Possibly, patient models could be loaded for retrospective analysis of the performance of MT.

The presented phantom simulations are not utilised further. However, to move further in this research, several tests have to be conducted. Foremost, testing should be done with heating. Different kinds of phantoms would be involved in the tests on imaging and heating to come. It would be of added value to have a simulation to design these tests. Also, they could be used as a ground truth or estimate. Therefore, the methodology and scripts for phantom simulations were developed and briefly presented here.

The presented results on the rotary symmetry and simulation-measurement correspondence rely on Imaging Tank 1, which is no more. Due to the limited time and already positive results, these results were not reproduced for Imaging Tank 2. However, it is not expected that this will yield largely different results. For the sake of completeness and the course of this research, it is advised to complete these tests.

The presented de-embedding methodology and script work well. However, the correspondence to a direct measurement is not as good as one might have hoped. It is a point for further research to see if, and how much, this impacts reconstruction. Also, it was found that the de-embedding measurement as well as the direct measurement are prone to errors, due to the constant moving, twisting and (dis)connecting of cables. Therefore, special care is advised.

When comparing the results for phase and amplitude on the de-embedding, it can be seen that the phase part works very well. Amplitude is naturally a bit more tricky because of all the different components, but it is of lesser relevance as we take a ratio measurement anyhow. Also, it might be that the direct measurement on antenna #3 is erroneous, as the wrapping of the phase seems off.
In the future, other aspects of the integration of microwave tomography in hyperthermia should be explored more deeply. Moreover, the accuracy and sensitivity of measurements and reconstruction should be characterized. This will prove crucial before moving on to clinical practice.

With clinical integration in mind, the speed of the reconstruction could also be improved. Though hyperthermia treatments typically last more than one hour, the half-hour that it takes to acquire the reconstruction is far from optimal. For example, if the patient's position can only be retrieved after 30 minutes, it is likely that the patient could have moved again. And even if the patient were to lay still, there is less time left to adapt the plan according to the found position. This will limit the therapeutic gain of microwave tomography.

To increase converging speeds, improvement of the reconstruction method is still ongoing and will likely improve the speed to less than ten minutes. Also, the inclusion of a-priori knowledge on patient position could be used. This can be done with an initial boundary/patient estimation. Some hyperthermia applicators have a built-in ultrasound probe that could be of use for this. The incorporation of this information was shortly researched but was then suspended due to limited time.

Conclusion

This research focussed on proving that the application of microwave tomography with a hyperthermia applicator is feasible. We have presented our results, which support the feasibility of the aforementioned application. With the use of a novel reconstruction algorithm, we can perform microwave tomography in a near-lossless coupling medium. A new imaging tank was built that is compatible with this reconstruction algorithm in terms of dimensions and physical properties. With the help of COMSOL simulations, the behaviour of this tank was modelled. On the hardware side, a switching matrix was brought back to life and its signal conduction was characterised. In order to use the setup in a clinical setting, the code and pipeline for usage were optimised. Moreover, a de-embedding implementation was realised. Hereby, the influence of any other component in the cascade but the imaging tank could be removed. This is essential for the accuracy and speed of the reconstruction. With these advancements, the clinical integration of microwave tomography has been brought closer. This could improve clinical outcomes and comfort for cancer patients undergoing hyperthermia treatment. Moreover, it may improve the quality and reproducibility of hyperthermia, improving its clinical acceptance.

References

[1] P. Schildkopf, O. J. Ott, B. Frey, M. Wadepohl, R. Sauer, R. Fietkau, and U. S. Gaipl, "Biological rationales and clinical applications of temperature controlled hyperthermia–implications for multimodal cancer treatments," *Current Medicinal Chemistry*, vol. 17, no. 27, pp. 3045–3057, 2010. 1

[2] N. van den Tempel, M. R. Horsman, and R. Kanaar, "Improving efficacy of hyperthermia in oncology by exploiting biological mechanisms," *International Journal of Hyperthermia: The Official Journal of European Society for Hyperthermic Oncology, North American Hyperthermia Group*, vol. 32, pp. 446–454, June 2016. 1, 2

[3] N. R. Datta, S. Rogers, S. G. Ordóñez, E. Puric, and S. Bodis, "Hyperthermia and radiotherapy in the management of head and neck cancers: A systematic review and meta-analysis," *International Journal of Hyperthermia*, vol. 32, pp. 31–40, Jan. 2016. Publisher: Taylor & Francis _eprint: https://doi.org/10.3109/02656736.2015.1099746. 2

[4] M. M. Paulides, P. R. Stauffer, E. Neufeld, P. F. Maccarini, A. Kyriakou, R. A. M. Canters, C. J. Diederich, J. F. Bakker, and G. C. Van Rhoon, "Simulation techniques in hyperthermia treatment planning," *International Journal of Hyperthermia*, vol. 29, pp. 346–357, June 2013. Publisher: Taylor & Francis _eprint: https://doi.org/10.3109/02656736.2013.790092. 3

[5] H. P. Kok and J. Crezee, "Hyperthermia Treatment Planning: Clinical Application and Ongoing Developments," *IEEE Journal of Electromagnetics, RF and Microwaves in Medicine and Biology*, vol. 5, pp. 214–222, Sept. 2021. Conference Name: IEEE Journal of Electromagnetics, RF and Microwaves in Medicine and Biology. 4

[6] IT'IS Foundation, "Tissue Properties Database V3.0," 2015. 4

[7] G. G. Bellizzi, T. Drizdal, G. C. van Rhoon, L. Crocco, T. Isernia, and M. M. Paulides, "The potential of constrained SAR focusing for hyperthermia treatment planning: analysis for the head & neck region," *Physics in Medicine and Biology*, vol. 64, p. 015013, Dec. 2018. 4

[8] T. V. Feddersen, J. A. Hernandez-Tamames, M. Franckena, G. C. van Rhoon, and M. M. Paulides, "Clinical Performance and Future Potential of Magnetic Resonance Thermometry in Hyperthermia," *Cancers*, vol. 13, p. 31, Jan. 2021. Number: 1 Publisher: Multidisciplinary Digital Publishing Institute. 4

[9] N. R. Datta, E. Stutz, S. Gomez, and S. Bodis, "Efficacy and Safety Evaluation of the Various Therapeutic Options in Locally Advanced Cervix Cancer: A Systematic

Review and Network Meta-Analysis of Randomized Clinical Trials," *International Journal of Radiation Oncology, Biology, Physics*, vol. 103, pp. 411–437, Feb. 2019. 4

[10] H. P. Kok, J. Crezee, N. A. P. Franken, L. J. A. Stalpers, G. W. Barendsen, and A. Bel, "Quantifying the combined effect of radiation therapy and hyperthermia in terms of equivalent dose distributions," *International Journal of Radiation Oncology, Biology, Physics*, vol. 88, pp. 739–745, Mar. 2014. 4

[11] J. Le Guevelou, M. E. Chirila, V. Achard, P. C. Guillemin, O. Lorton, J. W. E. Uiterwijk, G. Dipasquale, R. Salomir, and T. Zilli, "Combined hyperthermia and radiotherapy for prostate cancer: a systematic review," *International Journal of Hyperthermia*, vol. 39, pp. 547–556, Dec. 2022. Publisher: Taylor & Francis _eprint: https://doi.org/10.1080/02656736.2022.2053212. 4

[12] S. Gavazzi, A. L. H. M. W. van Lier, C. Zachiu, E. Jansen, J. J. W. Lagendijk, L. J. A. Stalpers, H. Crezee, and H. P. Kok, "Advanced patient-specific hyperthermia treatment planning," *International Journal of Hyperthermia*, vol. 37, pp. 992–1007, Jan. 2020. Publisher: Taylor & Francis _eprint: https://doi.org/10.1080/02656736.2020.1806361. 5

[13] N. K. Nikolova, "Microwave Imaging for Breast Cancer," *IEEE Microwave Magazine*, vol. 12, pp. 78–94, Dec. 2011. Conference Name: IEEE Microwave Magazine. 6

[14] S. Semenov, "Microwave tomography: review of the progress towards clinical applications," *Philosophical transactions. Series A, Mathematical, physical, and engineering sciences*, vol. 367, pp. 3021–3042, Aug. 2009. 6, 7

[15] L. Guo, A. Alqadami, and A. Abbosh, "Stroke Diagnosis Using Microwave Techniques: Review of Systems and Algorithms," *IEEE Journal of Electromagnetics, RF and Microwaves in Medicine and Biology*, vol. PP, pp. 1–14, Jan. 2022. 6

[16] N. Joachimowicz, I. Bolomey, C. Pichot, A. Franchois, I. Hugonint, L. Garnerot, and G. Gaboriaud, "Quantitative Microwave Tomography for Non-invasive Control of Hyperthermia. Preliminary Numerical Results," *The Journal of Photographic Science*, vol. 39, pp. 149–153, July 1991. Publisher: Taylor & Francis _eprint: https://doi.org/10.1080/00223638.1991.11737138. 6

[17] K. D. Paulsen, P. M. Meaney, M. J. Moskowitz, and J. R. Sullivan, "A dual mesh scheme for finite element based reconstruction algorithms," *IEEE transactions on medical imaging*, vol. 14, no. 3, pp. 504–514, 1995. 6

[18] P. M. Meaney, K. D. Paulsen, A. Hartov, and R. K. Crane, "An active microwave imaging system for reconstruction of 2-D electrical property distributions," *IEEE transactions on bio-medical engineering*, vol. 42, pp. 1017–1026, Oct. 1995. 6

[19] P. Meaney, K. Paulsen, A. Hartov, and R. Crane, "Microwave imaging for tissue assessment: initial evaluation in multitarget tissue-equivalent phantoms," *IEEE Transactions on Biomedical Engineering*, vol. 43, pp. 878–890, Sept. 1996. 6

[20] A. H. Golnabi, P. M. Meaney, N. R. Epstein, and K. D. Paulsen, "Microwave Imaging for Breast Cancer Detection: Advances in Three–Dimensional Image Reconstruction," *Conference proceedings : ... Annual International Conference of the IEEE*

Engineering in Medicine and Biology Society. IEEE Engineering in Medicine and Biology Society. Conference, vol. 2011, pp. 5730–5733, 2011. 6

[21] P. Meaney, M. Fanning, D. Li, S. Poplack, and K. Paulsen, "A clinical prototype of active microwave imaging of the breast," *Microwave Theory and Techniques, IEEE Transactions on*, vol. 48, pp. 1841–1853, Dec. 2000. 6

[22] P. M. Meaney, M. W. Fanning, R. M. di Florio-Alexander, P. A. Kaufman, S. D. Geimer, T. Zhou, and K. D. Paulsen, "Microwave Tomography in the Context of Complex Breast Cancer Imaging," *Conference proceedings : ... Annual International Conference of the IEEE Engineering in Medicine and Biology Society. IEEE Engineering in Medicine and Biology Society. Conference*, vol. 2010, pp. 3398–3401, 2010. 7

[23] A. Modiri, S. Goudreau, A. Rahimi, and K. Kiasaleh, "Review of breast screening: Toward clinical realization of microwave imaging," *Medical Physics*, vol. 44, pp. e446–e458, Dec. 2017. 7

[24] F. Yang, L. Sun, Z. Hu, H. Wang, D. Pan, R. Wu, X. Zhang, Y. Chen, and Q. Zhang, "A large-scale clinical trial of radar-based microwave breast imaging for Asian women: Phase I," in *2017 IEEE International Symposium on Antennas and Propagation & USNC/URSI National Radio Science Meeting*, pp. 781–783, July 2017. ISSN: 1947-1491. 7

[25] T. M. Grzegorczyk, P. M. Meaney, P. A. Kaufman, R. M. diFlorio Alexander, and K. D. Paulsen, "Fast 3-D Tomographic Microwave Imaging for Breast Cancer Detection," *IEEE transactions on medical imaging*, vol. 31, pp. 1584–1592, Aug. 2012. 7

[26] M. Baker-Fales, J. D. Gutiérrez-Cano, J. M. Catalá-Civera, and D. G. Vlachos, "Temperature-dependent complex dielectric permittivity: a simple measurement strategy for liquid-phase samples," *Scientific Reports*, vol. 13, p. 18171, Oct. 2023. Publisher: Nature Publishing Group. 11

[27] Tektronix, "Introduction to VNA Basics," Mar. 2017. 13

[28] D. M. Pozar, *Microwave Engineering, 4th Edition*. Wiley, 4th ed., Apr. 2012. 14, 15, 16

[29] R. . S. G. . C. KG, "R&S®ZNC vector network analyzer." 19

Appendices

A Switching Matrix schematic

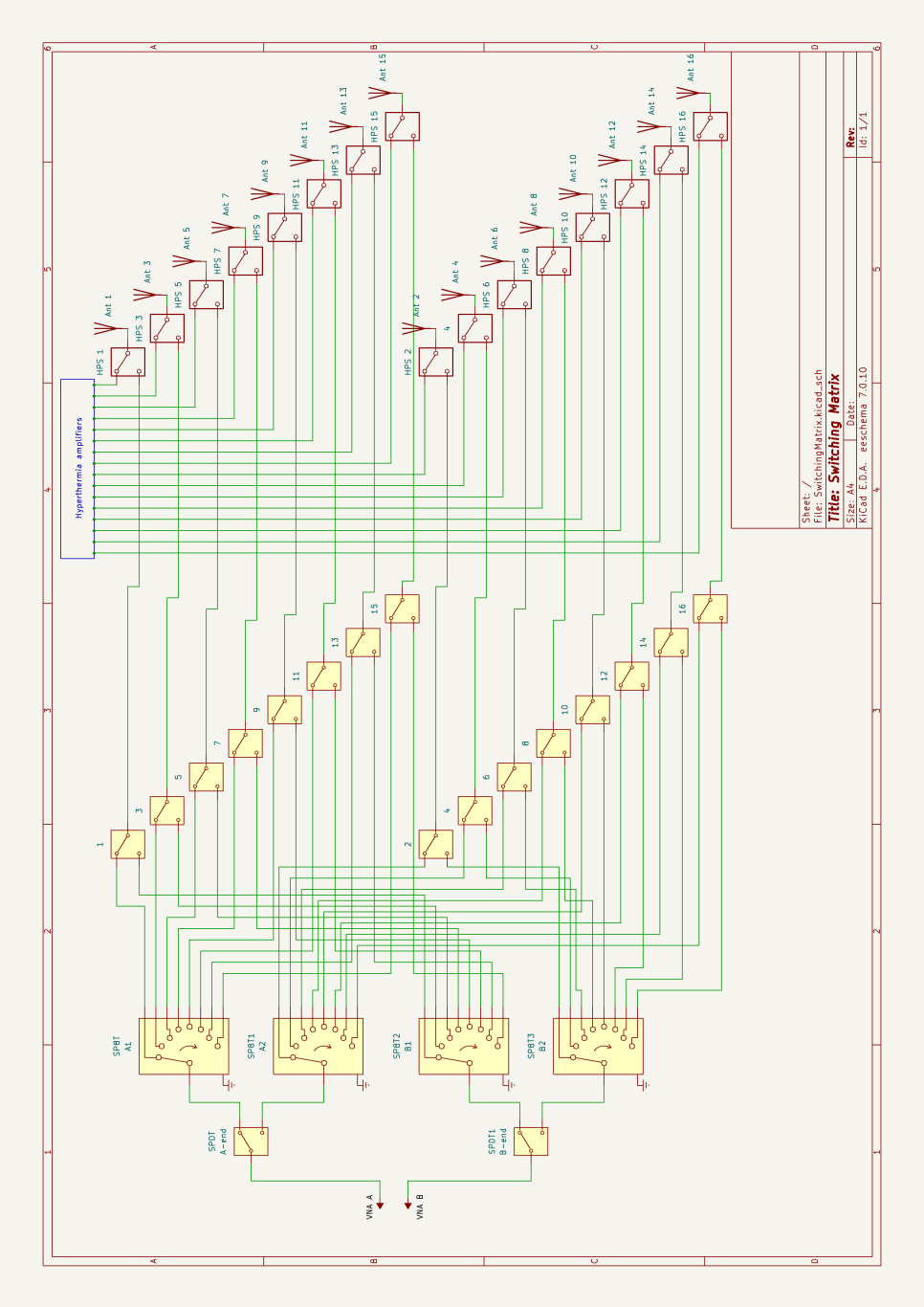

B Code measurements

single_measurement (through-matrix)

```
%%SINGLE_MEASUREMENT script for a single measurement through-
   matrix over all combinations with automated switching

close all;
clear variables;
clear all;
clc;

%% configuration

MEASUREMENTS_FOLDER = 'C:/Users/matth/OneDrive/Documenten/MEP/
   Measurements';
date = datestr(datetime('now'), 'yyyymmdd');
MEASUREMENT_NAME = [date ' (newTankMatchedPhantom)'];
addpath('../functions')

N_antennas = 16;
IMAGESHOW = 0;      % show images
VNAPLOT =   1;      % plot results as VNA portrays them
SAVE2x2 =   0;      % possibility to safe results as s2p files
DO_OVER =   1;      % redo possible faulty measurements
pauseTime = 0.3;

%% initialization

instrreset; % reset matlab's instrument connections
rohde_schwarz = visa('rs','TCPIP::169.254.118.228::INSTR' );%
   connect to VNA
rohde_schwarz.InputBufferSize= 128008;
fopen(rohde_schwarz); % open communication stream with VNA

fprintf(rohde_schwarz, 'calculate:parameter:define S11 ,s11'); %
   define measurements
fprintf(rohde_schwarz, 'calculate:parameter:define S21 ,s21');
fprintf(rohde_schwarz, 'calculate:parameter:define S12 ,s12');
fprintf(rohde_schwarz, 'calculate:parameter:define S22 ,s22');

%% obtain measurement configuration set manually

N_points = getPointCount(rohde_schwarz);      % number of
   measurement points to take
N_averages = getAverageCount(rohde_schwarz);  % number of
   measurements to average over. Important only if averaging is on
   .
```

```
[F_min, F_max] = getFrequencyRange(rohde_schwarz);    % finds
   frequencies to measure over

fprintf('N_points = %d\n', N_points);  %print setting gathered
   from VNA
fprintf('N_averages = %d\n', N_averages);
fprintf('F_min = %.3f GHz, F_max = %.3f GHz\n', F_min * 10 ^ -9,
   F_max * 10 ^ -9);

readMeasurement(rohde_schwarz, 'S11', N_averages); %initial
   measurement to verify connection

%% connect arduino

tic;
arduinoPort=serialport('COM7',9600);    % be sure to run
   Combinatorial_switch_mathced via Arduino IDE first
configureTerminator(arduinoPort,'CR/LF');
fprintf("Connecting Arduino took %f seconds\n",toc); % report
   connection time
pause(1);

writeline(arduinoPort,'8,9\n'); % ready the arduino
pause(0.1);

%% perform measurements

S = cell(N_antennas);
S11 = cell(N_antennas);

for j = 1 : N_antennas-1

    for i = j+1 : N_antennas

        fprintf('PORT 1 -> ANTENNA %d, PORT 2 -> ANTENNA %d ,   \
           n', j, i);

        writeline(arduinoPort,sprintf('%d, %d', j,i)); % sends
           arduino new connection to be made
        pause(pauseTime); % wait for physical conneciton

        % measure reflection (Port 1)
        fprintf('S%d,%d...', j, j);
        S11{i, j} = readMeasurement(rohde_schwarz, 'S11',
           N_averages);

        % measure foreward transmission
        fprintf('S%d,%d...', i, j);
```

```
            S{i, j} = readMeasurement(rohde_schwarz, 'S21',
               N_averages);

            % measure reflection (Port 2)
            fprintf('S%d,%d...', i, i);
            S11{j, i} = readMeasurement(rohde_schwarz, 'S22',
               N_averages);

            % measure backward transmission
            fprintf('S%d,%d...', j, i);
            S{j, i} = readMeasurement(rohde_schwarz, 'S12',
               N_averages);
            pause(0.01)
            fprintf('done.\n');

        end

    end

    fprintf('Completed.\n');

    f = F_min : (F_max - F_min) / (N_points - 1) : F_max; % create
       frequency axis

    F = cell(N_antennas); % create frequency matrix
    F11 = cell(N_antennas);
    for i = 1 : N_antennas
        for j = 1 : N_antennas
            F{i, j} = f;
            F11{i, j} = f;
        end
    end

    %% save results

    if ~isfolder(MEASUREMENTS_FOLDER)
        mkdir(MEASUREMENTS_FOLDER);
    end
    path = sprintf('%s/%s.mat', MEASUREMENTS_FOLDER, MEASUREMENT_NAME
       );
    save(path, 'F', 'S', 'F11', 'S11');

    %% redoing measurements

    if DO_OVER  % redoes measurements if expected deviation
        addpath('..\scripts\functions')
        disp('Redoing some measurments if needed')
```

```
    overview = evalMeasurements(S11,F,ceil(N_points/3),1); % will
        check if a measurement deviates a lot from average over
       all 120 based on reflection measurement.
    doOver = findDoOver(overview); % collects measurements to
       redo
    if length(doOver>1)
        fprintf("Redoing measurements on %d combinations", length
           (doOver))
        [S,S11] = redoMeas(doOver,S,S11, rohde_schwarz,
           arduinoPort, N_averages);
        fprintf('Redoing measurments done \nSaving...')
    end
end

path = sprintf('%s/%s[remeasured].mat', MEASUREMENTS_FOLDER,
   MEASUREMENT_NAME); % save redone measurmetn separately
save(path, 'F', 'S', 'F11', 'S11');

%% Disconnect and clear

fclose(instrfindall); % clear connections
delete(instrfindall);

clear arduinoPort
clear rohde_schwarz

%% built 2x2 S matrices
if SAVE2x2
   [...]
end

%% visualise
if IMAGESHOW
   [...]
end

%% plot as VNA
if VNAPLOT
    [...]
end
```

deembed_measurement

```
%% perform measurements

ways= {'A','B'};
```

```
f = F_min : (F_max - F_min) / (N_points - 1) : F_max; % create
   frequency axis
random=[7,8,7,8,7,8,5,4,5,4,5,4,5,4,5,4];
for i= 1: 2
    for j = 1 : N_antennas

    if i==1
        writeline(arduinoPort,sprintf('%d, %d', j,random(j)));%
           in firmware or '1\n')%
    else
        writeline(arduinoPort,sprintf('%d, %d', random(j),j));
    end
    pause (0.4);  % just enough time to make switch (seems the be
        the lower range of the saturation region)

    if string(ways(i)) == 'A'
        fprintf('Please connect Port 1 to SwMat input A and
           Antenna output %d to port 2. Then, press any key to
           continue\n',j);
    elseif string(ways(i)) == 'B'
        fprintf('Please connect Port 2 to SwMat input B and
           Antenna output %d to port 1. Then, press any key to
           continue\n',j);
    end

    %fprintf('Please connect Port 1 to SwMat input ' +string(ways
       (i)) + ' and Antenna output %d to port 2. Then, press any
       key to continue\n',j);

    pause

    % measure reflection (Port 1)
    S11 = readMeasurement(rohde_schwarz, 'S11', N_averages);

    % measure foreward transmission
    S21 = readMeasurement(rohde_schwarz, 'S21', N_averages);

    % measure reflection (Port 2)
    S22 = readMeasurement(rohde_schwarz, 'S22', N_averages);

    % measure backward transmission
    S12 = readMeasurement(rohde_schwarz, 'S12', N_averages);
    pause(0.01)
    fprintf(' Measurement done.\n');

    Sconcat=permute(cat(2,cat(3,S22,S21),cat(3,S12,S11)),[3,2,1])
       ; %build 2x2 S matrix
    Sparam2=sparameters(Sconcat,f,50);
```

```
    S2x2.(sprintf(string(ways(i)) +"_%02d",j))=Sparam2;
    end
    disp("Please disconnect the adapter from port 2 and connect
       it to port 1. /nAttach cable 2->B to port 2 and recalibrate
       ")
 end

fprintf('Completed.\n');
```

direct_measurement

```
%% combinations

combis = [1,6;2,5;3,4;7,10;8,16;9,15;11,13;12,14]'; % to be
   analysed, paths in Switching matrix, not antenna numbers per se

%% perform measurements

f = F_min : (F_max - F_min) / (N_points - 1) : F_max; % create
   frequency axis

for i=1:size(combis,2)

    fprintf('Please connect Port 1 to antenna %d  and Port 2 to %
       d\n', combis(1,i),combis(2,i) );
    pause

    % measure reflection (Port 1)
    S11 = readMeasurement(rohde_schwarz, 'S11', N_averages);

    % measure foreward transmission
    S21 = readMeasurement(rohde_schwarz, 'S21', N_averages);

    % measure reflection (Port 2)
    S22 = readMeasurement(rohde_schwarz, 'S22', N_averages);

    % measure backward transmission
    S12 = readMeasurement(rohde_schwarz, 'S12', N_averages);
    pause(0.01)
    fprintf(' Measurement done.\n');

    Sconcat=permute(cat(2,cat(3,S22,S21),cat(3,S12,S11)),[3,2,1])
       ; %build 2x2 S matrix
    Sparam2=sparameters(Sconcat,f,50);
    S2x2.(sprintf("Com%02d_%02d",combis(1,i),combis(2,i)))=
       Sparam2;
 end
```

```
fprintf('Completed.\n');
```

C Imaging Tank 1 de-embedding

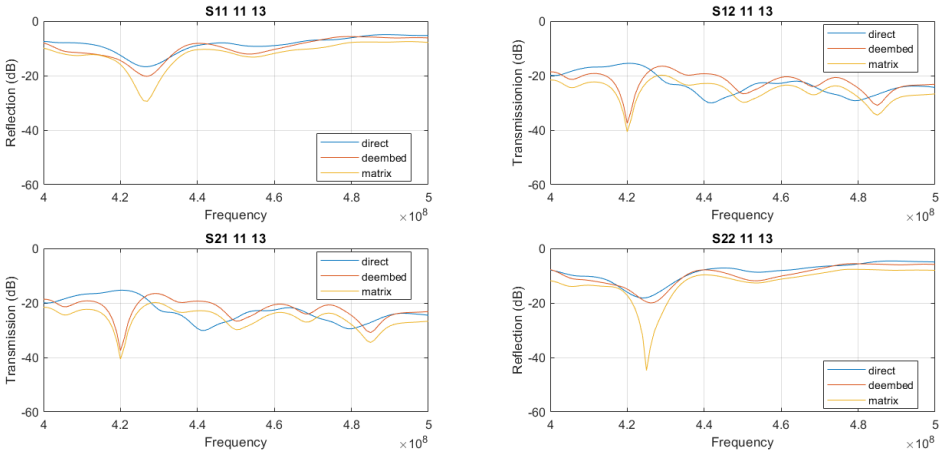

(a)

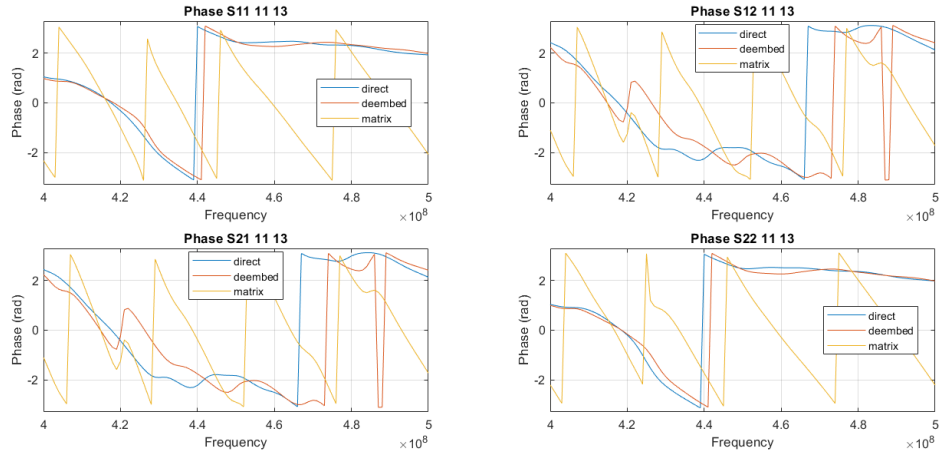

(b)

Comparison of direct, de-embedded matrix and through-matrix measurements for antennas #11 and #13 of Imaging Tank 1. (a): Magnitude versus frequency for all four S-parameters. (b) Phase versus frequency for all four S-parameters.

D De-embedding path measurements

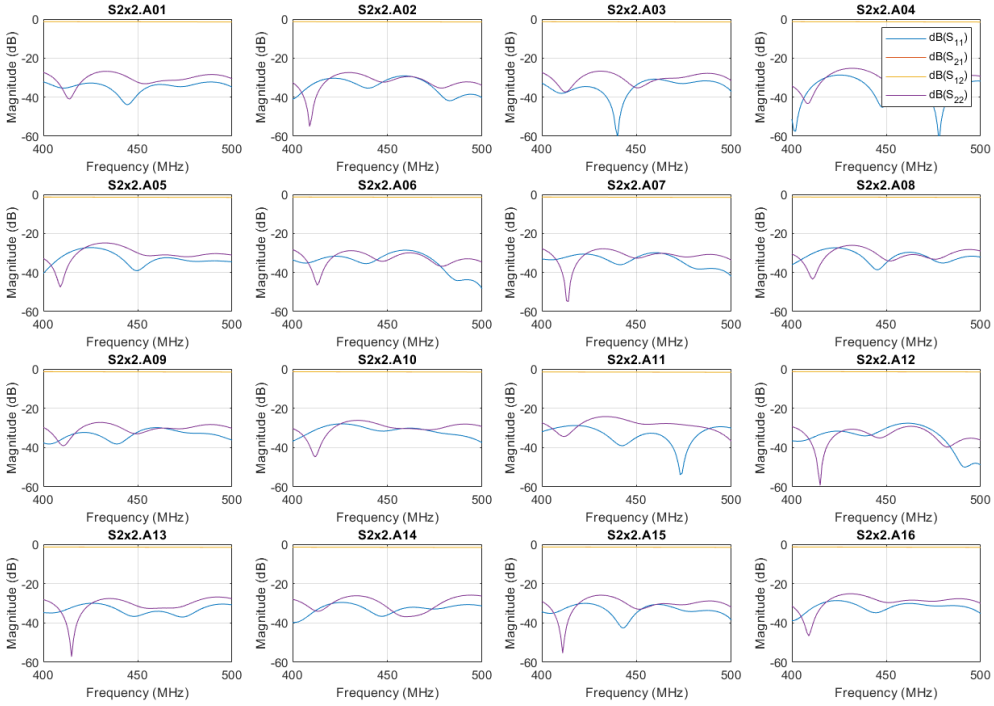

(a)

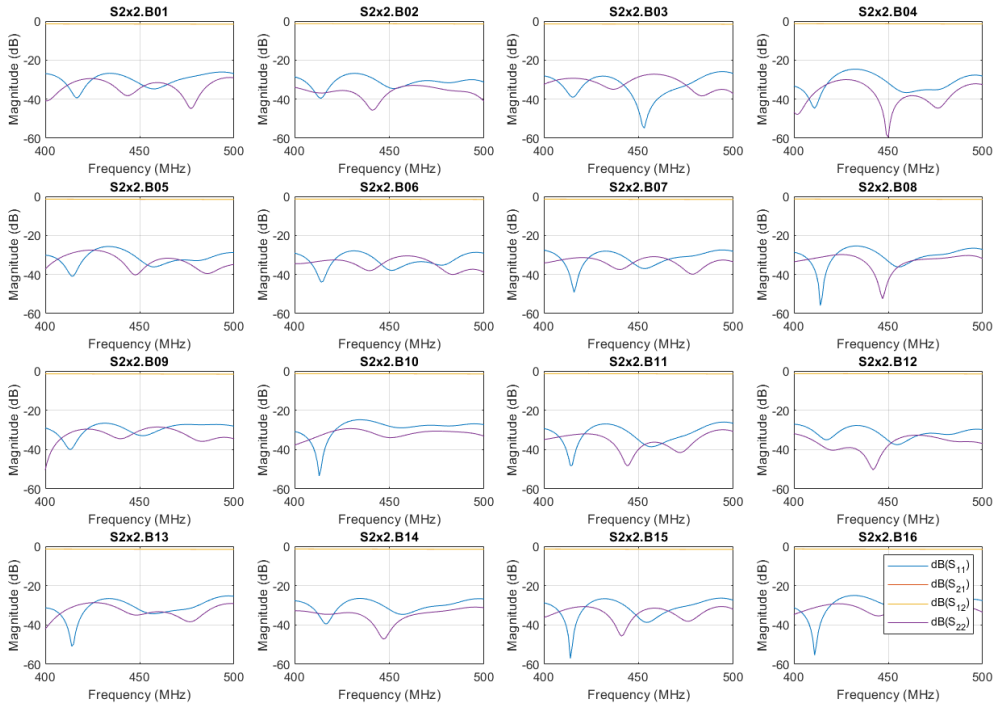

(b)

De-embedding measurements for 16 paths. (a): Paths through port A/1 in the SwMat and VNA. (b) Paths through port B/2 in the SwMat and VNA.